

Gravitational-wave Observations Suggest Most Black Hole Mergers Form in Triples

JAKOB STEGMANN ¹, FABIO ANTONINI ², ALEKSANDRA OLEJAK ¹, SYLVIA BISCOVEANU ³, VIVIEN RAYMOND,²
STEFANO RINALDI ⁴ AND ELIZABETH FLANAGAN²

¹*Max Planck Institute for Astrophysics, Karl-Schwarzschild-Str. 1, 85741 Garching, Germany*

²*Gravity Exploration Institute, School of Physics and Astronomy, Cardiff University, Cardiff, CF24 3AA, UK*

³*Department of Physics, Princeton University, Princeton, NJ 08544, USA*

⁴*Institut für Theoretische Astrophysik, ZAH, Universität Heidelberg, Albert-Ueberle-Str. 2, 69120 Heidelberg, Germany*

ABSTRACT

The spin-orbit tilt angles $\theta_{1(2)}$ of merging stellar-mass black holes provide key insights into their astrophysical origin. Non-parametric population modelling of [The LIGO, Virgo, and KAGRA Collaborations \(2025a\)](#) shows that the spin-orbit tilt distribution of mergers in the latest Gravitational-Wave Transient Catalog 4.0 exhibits a global peak at near-perpendicular directions $\cos\theta_{1(2)} \approx 0$. Here, we recover this feature using hierarchical Bayesian inference with parametric models that are tailored to enhance the diagnostic power about astrophysical formation channels. We find that the spin distribution of the low-mass bulk of the binary black hole merger population ($m_1 \lesssim 44.3_{-4.6}^{+8.7} M_\odot$) can be well-modelled by a dominant Gaussian component that peaks at $\cos\theta_{1(2)} \approx 0$, possibly mixed with a subdominant isotropic component. Models that include a component with spins preferentially aligned with the orbit are disfavoured by current data (with Bayes factors $|\Delta \ln \mathcal{B}| \approx 1$ to 3) and constrain its contribution to be likely small ($\xi \sim \mathcal{O}(1)\%$), although large contributions cannot yet be ruled out with certainty. If these findings are reinforced by more detections, they would challenge any major contribution from the traditional isolated-binary formation scenario yielding closely aligned spins. Instead, the dominant component with near-perpendicular spins matches expectations from the evolution of isolated massive stellar triples in the galactic field, where the Lidov–Kozai effect naturally produces a unique overabundance of mergers with $\cos\theta_{1(2)} \approx 0$.

1. INTRODUCTION

A decade after the first direct detection of gravitational waves from merging binary black holes ([B. P. Abbott et al. 2016](#)), the observational sample detected by the LIGO–Virgo–KAGRA (LVK) interferometers has grown to about two hundred of these events ([J. Aasi et al. 2015](#); [F. Acernese et al. 2015](#); [Y. Aso et al. 2013](#); [K. Somiya 2012](#); [B. P. Abbott et al. 2018](#); [T. Akutsu et al. 2020](#); [The LIGO, Virgo, and KAGRA Collaborations 2025b](#)). Yet, a central question remains open: What are the formation mechanisms behind the observed mergers of black holes?

Resolving this question has become a major challenge in gravitational-wave astronomy as most proposed binary black hole formation channels—such as those arising from isolated binary-star evolution ([K. Belczynski et al. 2016](#)), active galactic nuclei ([N. C. Stone et al. 2017](#)), or ultra-wide binaries perturbed by the Galaxy ([J. Stegmann et al. 2024](#))—are notoriously difficult to

model in a predictive way (e.g., [D. Gerosa et al. 2018](#); [V. Baibhav & V. Kalogera 2024](#)). Their outcomes depend on numerous uncertain assumptions, making their predictions highly flexible; with sufficient tuning, they can be made to reproduce a wide range of features in gravitational-wave observations.

Among all proposed formation channels, the evolution of triples—which are by far the most abundant observed configuration of massive black hole progenitor stars ([M. Moe & R. Di Stefano 2017](#); [S. S. R. Offner et al. 2023](#))—stands out by making a unique, testable prediction for the spin orientation of merging black holes. In this scenario, the gravitational perturbation from a distant companion drives large-amplitude eccentricity oscillations (the “Lidov–Kozai” effect) of black holes formed in the inner binary ([H. V. Zeipel 1909](#); [M. L. Lidov 1962](#); [Y. Kozai 1962](#); [S. Naoz 2016](#)). Efficient gravitational-wave emission during close pericentre passages can then lead the binary to inspiral and merge ([K. Silsbee & S. Tremaine 2017](#); [F. Antonini et al. 2017](#); [E. Grishin et al. 2018](#); [B. Liu & D. Lai 2018](#); [F. Antonini et al. 2018](#); [C. L. Rodriguez & F. Antonini 2018](#); [A. Mangipudi](#)

et al. 2022; J. Stegmann et al. 2022a; A. Vigna-Gómez et al. 2025; A. Dorozsmai et al. 2025; J. Stegmann & J. Klencki 2025). Under well-defined conditions, the combined action of Lidov–Kozai oscillations, gravitational-wave emission, and relativistic spin precession drives the component spins to flip into the orbital plane (F. Antonini et al. 2018; B. Liu & D. Lai 2018; C. L. Rodriguez & F. Antonini 2018; Y. Su et al. 2021), producing an overall excess of systems with spin–orbit misalignments near perpendicular (cf. Section 4). This configuration is so unusual that other formation channels typically require additional, ad hoc assumptions to reproduce it (e.g., J. Stegmann & F. Antonini 2021; T. M. Tauris 2022; V. Baibhav & V. Kalogera 2024; M. P. Vaccaro et al. 2024). The triple scenario therefore provides a robust formation pathway with a clear, falsifiable prediction.

Tentative evidence for a global peak in the binary black hole population at $\cos\theta \approx 0$ —corresponding to a spin–orbit tilt angle of about 90° —was identified in analyses of earlier LVK catalogues through parametric modelling in S. Vitale et al. (2022) and was subsequently corroborated with more agnostic spin models (B. Edelman et al. 2023; J. Golomb & C. Talbot 2023). Support for this feature has strengthened with the Gravitational-Wave Transient Catalog 4.0 (GWTC-4.0; The LIGO and Virgo Collaborations 2022; The LIGO, Virgo, and KAGRA Collaborations 2023a, 2025c,b,a, see Figure 7 in the latter), particularly in the non-parametric (“weakly modelled”) B-spline population model (B. Edelman et al. 2023), which makes minimal *a priori* assumptions, but can be difficult to interpret astrophysically. The LVK’s parametric (“strongly modelled”) default spin-tilt model (The LIGO, Virgo, and KAGRA Collaborations 2025a) also recovers weak evidence for this peak. Here we aim to assess and interpret this feature using a more astrophysically motivated parametric framework, that allows direct comparison with predictions from formation channels.

2. METHODS

While many studies have shown that the population spin–tilt distribution is a powerful discriminator of black hole formation channels (S. Vitale et al. 2017; S. Stevenson et al. 2017; C. Talbot & E. Thrane 2017; S. Vitale et al. 2022), tilt measurements for individual events carry large uncertainties (S. Vitale et al. 2014; G. Pratten et al. 2020; S. Biscoveanu et al. 2021), limiting population-level inference (S. J. Miller et al. 2024; S. Vitale & M. Mould 2025). Population constraints have therefore often relied on the effective spin $\chi_{\text{eff}} = \chi_1 \cos\theta_1 + q\chi_2 \cos\theta_2 / (1 + q)$, where $\chi_{1(2)}$ and

$\theta_{1(2)}$ denote the component spin magnitudes and tilt angles, respectively, and $0 < q \leq 1$ is the binary mass ratio (T. Damour 2001). While χ_{eff} is more precisely measured, its inferred population distribution peaks near zero (S. Miller et al. 2020; J. Roulet et al. 2021; S. Banagiri et al. 2025; The LIGO, Virgo, and KAGRA Collaborations 2025a). This is intrinsically ambiguous: it can arise from small spin magnitudes or from substantial spin-orbit misalignment, and it is further compounded by the mass-weighted combination of both components. This motivates investigating the population distribution of individual spin magnitudes and tilts directly, rather than relying on χ_{eff} alone. In what follows, we therefore employ a hierarchical Bayesian inference method (e.g., I. Mandel et al. 2019) to infer hyper-parameters describing the component spin properties of the binary black hole merger population.

We use the `GWPopulation` code (C. Talbot et al. 2019; C. Talbot et al. 2025) and the public detector sensitivity estimates (R. Essick et al. 2025; The LIGO, Virgo, and KAGRA Collaborations 2025d) and individual event posteriors from GWTC-4.0 (The LIGO and Virgo Collaborations 2022; The LIGO, Virgo, and KAGRA Collaborations 2023a, 2025c). In using `GWPopulation`, we limit the variance of the Monte Carlo–estimated log-likelihood to be below 1 and use the posterior samples obtained with the `NRSur7dq4` waveform model (V. Varma et al. 2019) where available for new events in GWTC-4.0, the mixed-waveform samples otherwise, and the `IMRPhenomXPHM` waveform samples (G. Pratten et al. 2021; M. Colleoni et al. 2025) for all events that appear in previous catalogs. Our method is exemplified in a public script⁵ accompanying this work and detailed in the following.

In order to streamline our notation, we introduce two helper functions

$$\pi_\chi(\chi_i|\mu_\chi, \sigma_\chi) = \mathcal{N}_{[0,1]}(\chi_1|\mu_\chi, \sigma_\chi)\mathcal{N}_{[0,1]}(\chi_2|\mu_\chi, \sigma_\chi), \quad (1)$$

$$\pi_t(\cos\theta_i|\mu_t, \sigma_t) = \mathcal{N}_{[-1,1]}(\cos\theta_1|\mu_t, \sigma_t) \times \mathcal{N}_{[-1,1]}(\cos\theta_2|\mu_t, \sigma_t), \quad (2)$$

where $\mathcal{N}_{[a,b]}(x|\mu, \sigma)$ is a truncated Gaussian distribution within $a \leq x \leq b$ and μ and σ are its mean and standard deviation, respectively. Using Equations (1) and (2) we

⁵ <https://github.com/stegmaja/black-hole-spin-orbit-tilts>

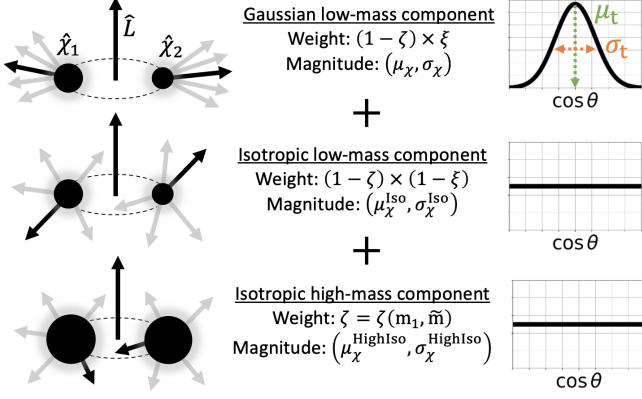


Figure 1. Schematic overview of the parametric spin population model described in Equation (3). Below a mass cut-off $m_1 \lesssim \tilde{m}$ the population is described by a mixture between a component whose spin directions $\cos \theta_{1(2)} = \hat{\chi}_{1(2)} \cdot \hat{\mathbf{L}}$ follow a truncated Gaussian distribution (mixing fraction ξ) and a component with isotropic spin directions (mixing fraction $1 - \xi$). Above $m_1 \gtrsim \tilde{m}$ the spins also follow an isotropic distribution. Each of the three components are allowed to follow different spin magnitude distributions.

define the distribution function

$$\pi(\chi_i, \cos \theta_i | \Lambda) = (1 - \zeta) \left[\xi \pi_t(\cos \theta_i | \mu_t, \sigma_t) \pi_\chi(\chi_i | \mu_\chi, \sigma_\chi) + \frac{1 - \xi}{4} \pi_\chi(\chi_i | \mu_\chi^{\text{Iso}}, \sigma_\chi^{\text{Iso}}) \right] + \frac{\zeta}{4} \pi_\chi(\chi_i | \mu_\chi^{\text{HighIso}}, \sigma_\chi^{\text{HighIso}}), \quad (3)$$

$$\{\zeta, \xi, \mu_t, \sigma_t, \mu_\chi, \sigma_\chi, \mu_\chi^{\text{Iso}}, \sigma_\chi^{\text{Iso}}, \mu_\chi^{\text{HighIso}}, \sigma_\chi^{\text{HighIso}}\} \in \Lambda$$

where $0 \leq \xi \leq 1$ is a mixing fraction describing the Gaussian component (while $1 - \xi$ is isotropic), $\zeta = \zeta(m_1; \tilde{m})$ is defined below and describes a mass-dependent transition to a fully isotropic component above $m_1 \gtrsim \tilde{m}$, and all μ 's and σ 's define means and standard deviations of the truncated normal distributions in Equations (1) and (2), respectively. In Figure 1, we provide a schematic overview of the various components involved in Equation (3). We summarise our modelling of the black hole mass and redshift distributions in Appendix A.

Equation (3) is used to investigate population models that reflect merger contributions from various astrophysical formation channels. An isotropic component is expected from binary black hole mergers formed through close few-body encounters in dense environments such as star clusters (e.g., C. L. Rodriguez et al. 2016). Mergers from the evolution of isolated binary and triple systems are expected to have preferentially aligned (V. Kalogera 2000; W. M. Farr et al. 2017; D. Gerosa et al. 2018; K. Belczynski et al. 2020; S. S. Bavera et al. 2020; A. Olejak & K. Belczynski 2021; F. S. Broekgaarden et al. 2022) or near-perpendicular spin-orbit orientations (F.

Antonini et al. 2018; B. Liu & D. Lai 2018), respectively, and can be reflected by the Gaussian component with appropriate μ_t and σ_t (cf. Section 4). Meanwhile, mergers assembled in active galactic nucleus disks are less certain but generally expected to inherit a preferred axis set by the disk angular momentum (Y. Yang et al. 2019; M. P. Vaccaro et al. 2024).

Thus, we introduce a set of parametric models whose properties are summarised in Table 1 and priors on the population parameters are defined at the end of this section. In the **Gaussian** and **Aligned** models we assume that the spin-orbit tilts can be described by a single truncated Gaussian whose location is allowed to be free within $-1 \leq \mu_t \leq 1$ or enforced at alignment $\mu_t = 1$, respectively. In these single-component models we impose $\zeta = 0$ and $\xi = 1$. In the next set of models **Gaussian + Isotropic**, **Uniform Gaussian + Isotropic**, and **Aligned + Isotropic** we allow for a free mixing with an isotropic component by allowing $0 \leq \xi \leq 1$. In these models, the Gaussian and isotropic components are allowed to follow different spin magnitude distributions each parametrised by truncated Gaussians with (μ_χ, σ_χ) and $(\mu_\chi^{\text{Iso}}, \sigma_\chi^{\text{Iso}})$, respectively. If both components are thought to represent two different astrophysical subpopulations, e.g., from the evolution of isolated stellar few-body systems (binaries, triples, etc.) and from few-body encounters in dense environments (e.g., globular clusters), respectively, there is *a priori* no reason to assume they should follow the same spin magnitude distribution. This is different from the default modelling of **The LIGO, Virgo, and KAGRA Collaborations (2025a)**, which enforces the same spin magnitude distribution in both components. To test the consequences of this assumption, we include two models **LVK Gaussian + Isotropic** and **LVK Uniform Gaussian + Isotropic**, where we replace $(\mu_\chi^{\text{Iso}}, \sigma_\chi^{\text{Iso}})$ by (μ_χ, σ_χ) .

Finally, F. Antonini et al. (2025a,b) identify a transition to an isotropic high-spin population for primary masses above a mass threshold $\tilde{m} = 45_{-4}^{+6} M_\odot$, which they interpret as evidence for a high-mass tail produced through hierarchical black hole mergers (e.g., C. L. Rodriguez et al. 2019; D. Gerosa & M. Fishbach 2021). Consistently, Y.-Z. Wang et al. (2022) identify a similar transition to a higher-spin population at $46.1_{-5.1}^{+5.6} M_\odot$ based on GWTC-3 data. Here, we focus on the lower-mass bulk of the astrophysical merger population, but ensure that our analysis is not contaminated by the distinct spin properties of the high-mass population. Therefore, we introduce a **Gaussian + Isotropic + Cut** model, in which

$$\zeta(m_1, \tilde{m}) = \frac{1}{1 + \exp[k(\tilde{m} - m_1)]} \quad (4)$$

Models	Definitions				$Y_{\text{vs. aligned}}$	$Y_{\text{vs. anti-aligned}}$	$\Delta \ln \mathcal{B}$		
(1)	$\zeta = 0$	$\xi = 1$	$-1 \leq \mu_t \leq 1$	$\sigma_t \sim \mathcal{N}_{[0.1,4]}$	$3.0^{+3.6}_{-1.5}$	$10.8^{+23.9}_{-6.7}$	-10.1		
(2)	$\zeta = 0$	$\xi = 1$	$\mu_t = 1$	$\sigma_t \sim \mathcal{N}_{[0.1,4]}$	$0.7^{+0.1}_{-0.1}$	$2.5^{+0.7}_{-0.5}$	-13.2		
(3)	$\zeta = 0$	$0 \leq \xi \leq 1$	$-1 \leq \mu_t \leq 1$	$\sigma_t \sim \mathcal{N}_{[0.1,4]}$	$1.4^{+1.5}_{-0.4}$	$2.7^{+3.3}_{-1.5}$	-6.3		
(4)	$\zeta = 0$	$0 \leq \xi \leq 1$	$-1 \leq \mu_t \leq 1$	$\sigma_t \sim \mathcal{U}_{[0.1,4]}$	$1.0^{+0.2}_{-0.1}$	$1.2^{+1.0}_{-0.2}$	-6.9		
(5)	$\zeta = 0$	$0 \leq \xi \leq 1$	$\mu_t = 1$	$\sigma_t \sim \mathcal{N}_{[0.1,4]}$	$0.8^{+0.1}_{-0.1}$	$1.1^{+0.1}_{-0.1}$	-7.2		
(6)	$\zeta = 0$	$0 \leq \xi \leq 1$	$-1 \leq \mu_t \leq 1$	$\sigma_t \sim \mathcal{N}_{[0.1,4]}$	$\mu_\chi = \mu_\chi^{\text{Iso}}$	$\sigma_\chi = \sigma_\chi^{\text{Iso}}$	$2.5^{+2.5}_{-1.2}$	$4.5^{+5.7}_{-2.3}$	-11.2
(7)	$\zeta = 0$	$0 \leq \xi \leq 1$	$-1 \leq \mu_t \leq 1$	$\sigma_t \sim \mathcal{U}_{[0.1,4]}$	$\mu_\chi = \mu_\chi^{\text{Iso}}$	$\sigma_\chi = \sigma_\chi^{\text{Iso}}$	$1.2^{+2.0}_{-0.3}$	$2.3^{+4.2}_{-1.1}$	-14.7
(8)	$\zeta(m_1, \tilde{m})$	$0 \leq \xi \leq 1$	$\mu_t = 1$	$\sigma_t \sim \mathcal{N}_{[0.1,4]}$			$0.9^{+0.1}_{-0.1}$	$1.1^{+0.7}_{-0.1}$	-1.6
(9)	$\zeta(m_1, \tilde{m})$	$0 \leq \xi \leq 1$	$-1 \leq \mu_t \leq 1$	$\sigma_t \sim \mathcal{N}_{[0.1,4]}$			$1.7^{+1.9}_{-0.7}$	$3.4^{+4.7}_{-1.9}$	0.0

Models: (1) **Gaussian** (2) **Aligned** (3) **Gaussian + Isotropic** (4) **Uniform Gaussian + Isotropic** (5) **Aligned + Isotropic** (6) **LVK Gaussian + Isotropic** (7) **LVK Uniform Gaussian + Isotropic** (8) **Aligned + Isotropic + Cut** (9) **Gaussian + Isotropic + Cut**

Table 1. Overview of parametric spin models studied in this work. The truncated normal distribution $\mathcal{N}_{[0.1,4]}$ used as a prior for σ_t in most models is assuming a mean and standard deviation of $\mu = 0$ and $\sigma = 1/2$, respectively. The two LVK models enforce that the Gaussian and isotropic components are following the same spin magnitude distribution, i.e., μ_χ^{Iso} and σ_χ^{Iso} in Equation (3) are replaced by μ_χ and σ_χ , respectively. Other model specifications are detailed in Section 2. The last three columns contain the excess fractions defined in Equations (5) and (6) for $\delta = 0.1$ and resulting Bayes factors relative to the **Gaussian + Isotropic + Cut** model, which are discussed in Section 3.

is a sigmoid function that smoothly transitions from the **Gaussian + Isotropic** model at low primary masses $m_1 \lesssim \tilde{m}$ to an isotropic component with separate spin magnitude distribution ($\mu_\chi^{\text{HighIso}}, \sigma_\chi^{\text{HighIso}}$) at high masses $m_1 \gtrsim \tilde{m}$. Another model **Aligned + Isotropic + Cut** additionally enforces $\mu_t = 1$. As a default, we fix $\tilde{k} = 1$ in all our models which incorporate the mass cut. We have also tested one variant of the **Gaussian + Isotropic + Cut** model, where we allow \tilde{k} to be a free hyper-parameter of the model between 0.1 and 2.0 (where larger values of \tilde{k} lead to a sharper transition in mass). As a result, we found that $\tilde{k} = 0.9^{+0.7}_{-0.6}$ is poorly constrained with a posterior distribution which is largely consistent with the prior on \tilde{k} , which we assumed to be uniform. As shown in Appendix B, we also found all other posterior distributions of the model parameters to be largely similar between the runs with free and a fixed $\tilde{k} = 1$.

We assume uniform distributions, $\mathcal{U}_{[a,b]}$ between a and b , for the priors of most model hyper-parameters:

- $\mathcal{U}_{[0,1]}$ for $\mu_\chi, \mu_\chi^{\text{Iso}}, \mu_\chi^{\text{HighIso}}$, and ξ ,
- $\mathcal{U}_{[0.1,1]}$ for $\sigma_\chi, \sigma_\chi^{\text{Iso}}$, and $\sigma_\chi^{\text{HighIso}}$,
- $\mathcal{U}_{[10,100]}$ for \tilde{m}/M_\odot .

In the **Uniform Gaussian + Isotropic** and **LVK Uniform Gaussian + Isotropic** models we also assume a uniform prior $\mathcal{U}_{[0.1,4]}$ for σ_t , similar to population models of [The LIGO, Virgo, and KAGRA Collaborations \(2025a\)](#). In all other models we assume $\mathcal{N}_{[0.1,4]}(\mu = 0, \sigma = 1/2)$, as wide spin tilt distributions (e.g., reflected in a uniform prior up to $\sigma_t = 4$) are

inconsistent with most astrophysical models, which instead tend to exhibit more pronounced peaks and are better modelled by a width of $\sigma \approx 1/2$ or less (e.g., [V. Baibhav & V. Kalogera 2024](#), and astrophysical models in Figure 2 below).

3. RESULTS

At first, we quantify the statistical significance of the global peak at $\cos \theta \approx 0$ in the non-parametric B-Spline model of [The LIGO, Virgo, and KAGRA Collaborations \(2025a\)](#). We follow a similar approach as [S. Vitale et al. \(2022\)](#) and define

$$Y_{\text{vs. aligned}}(\delta) = \frac{p(\cos \theta \in [-\delta/2, \delta/2])}{p(\cos \theta \in [1 - \delta, 1])}, \quad (5)$$

$$Y_{\text{vs. anti-aligned}}(\delta) = \frac{p(\cos \theta \in [-\delta/2, \delta/2])}{p(\cos \theta \in [-1, -1 + \delta])}, \quad (6)$$

to quantify the excess of near-perpendicular spin-orbit angles within $\pm \delta/2$ compared to near-aligned ($\cos \theta \in [1 - \delta, 1]$) and near-anti-aligned configurations ($\cos \theta \in [-1, -1 + \delta]$), respectively. For the public hyper-parameter posterior samples of the B-Spline model ([The LIGO, Virgo, and KAGRA Collaborations 2025a,e](#)) and $\delta = 0.1$ we find $Y_{\text{vs. aligned}} = 1.5^{+0.7}_{-0.5}$ and $Y_{\text{vs. anti-aligned}} = 2.5^{+1.8}_{-1.0}$, which suggest a statistically significant excess at $\cos \theta \approx 0$ and a skewness to positive values of $\cos \theta$.

Concerning our parametric models, we find that this spin distribution is best represented by **Gaussian + Isotropic + Cut** model which outperforms all other models, but **Aligned + Isotropic + Cut**, strongly ([H. Jeffreys 1939](#); [R. E. Kass & A. E. Raftery 1995](#)) with

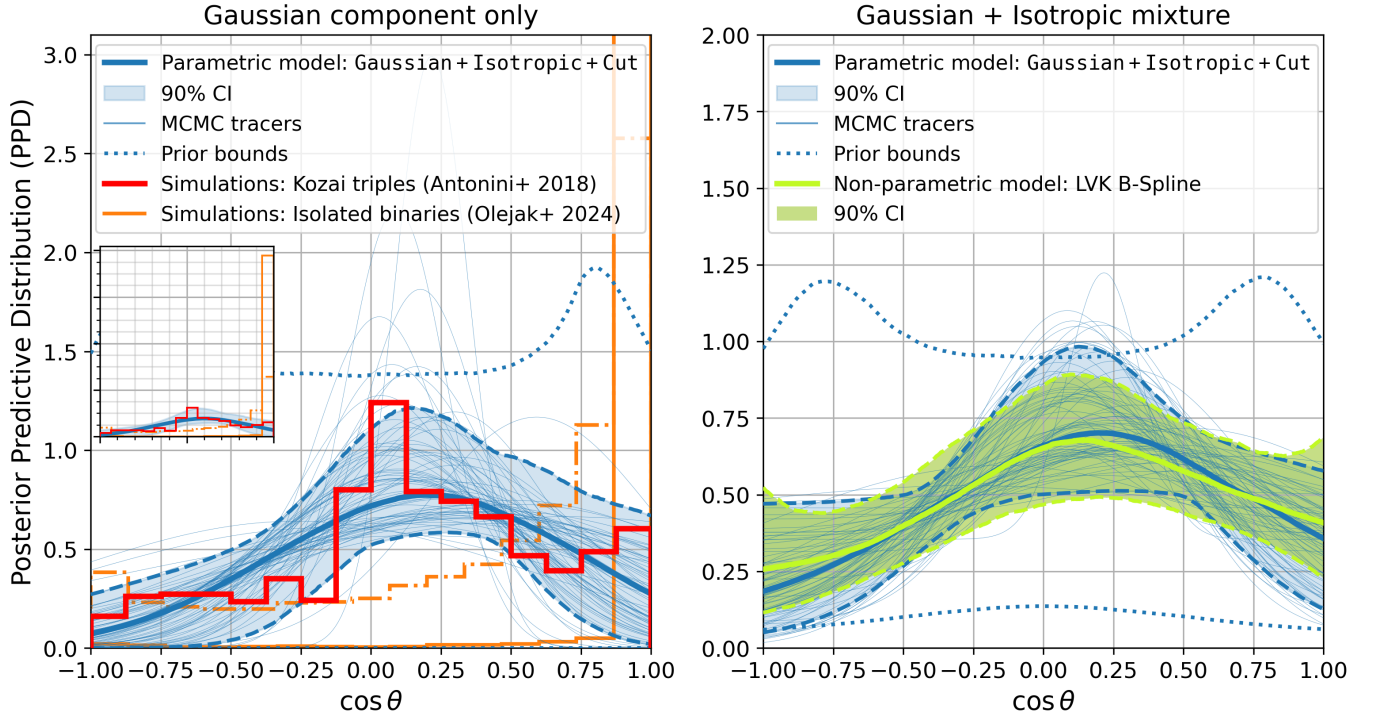


Figure 2. Posterior predictive distribution (PPD) of the black hole spin tilts of the low-mass population ($m_1 \lesssim \tilde{m} = 44.3^{+8.6}_{-4.6} M_\odot$) in our parametric **Gaussian + Isotropic + Cut** model (blue). The PPD is constructed by taking the quantiles (median indicated by dashed lines, 90% interval by shaded envelope) across MCMC samples (thin lines). The left panel shows the PPD of only the low-mass Gaussian component, the right panel includes the low-mass isotropic component. The green colour shows the non-parametric B-Spline model of [The LIGO, Virgo, and KAGRA Collaborations \(2025a,e\)](#). In both panels, the dotted blue lines indicate the prior bounds (90%), i.e., they show the PPDs if all hyperparameters are drawn from their priors. The red line shows simulation outcomes of binary black hole mergers which are caused by the Lidov–Kozai effect in hierarchical triples ([F. Antonini et al. 2018](#)). The orange lines show simulation outcomes of binary black hole mergers from isolated binary star evolution ([A. Olejak et al. 2024](#)) assuming high natal kicks at black hole formation that are drawn from a Maxwellian velocity distribution with $\sigma = 133 \text{ km s}^{-1}$ (dash-dotted) or natal kicks lowered by fallback ([C. L. Fryer et al. 2012](#)) with $\sigma = 265 \text{ km s}^{-1}$ (solid). Since we cut the y-axis, the small inset (linear axes) shows that the orange models are strongly concentrated at $\cos \approx 1$. In the right panel, the binary black hole sketch depicts a merger with $\cos \theta_{1(2)} \approx 0$, where, for visualisation purposes, we pick near-opposite in-plane directions.

Bayes factors of $|\Delta \ln \mathcal{B}| > 6.3$ (summarised in the last column of Table 1). Evidences for each model are calculated using the *Dynesty* nested sampler ([J. S. Speagle 2020](#)), with error estimates on the order of $\mathcal{O}(0.1)$ in log-evidence, much smaller than the log Bayes factors we calculate in favour of the **Gaussian + Isotropic + Cut** model. This aligns with the astrophysical expectation of an isotropic component from dense environments above some mass threshold and a combination with mergers from stellar evolution processes below the threshold (e.g., [C. L. Rodriguez et al. 2019](#); [D. Gerosa & M. Fishbach 2021](#)). Allowing for a free Gaussian is always statistically preferred over enforced spin-orbit alignment. Evidence of **Gaussian + Isotropic + Cut** against the aligned counterpart **Aligned + Isotropic + Cut** is positive but not decisive ($|\Delta \ln \mathcal{B}| = 1.6$). However, in Appendix C we argue that the contribution from the aligned component in the **Aligned + Isotropic +**

Cut needs to be small and gets more strongly disfavoured if very wide opening angles are excluded. Moreover, aligned models consistently disagree with the inferred excess fractions of the non-parametric model above, as summarised in Table 1. Thus, in what follows we focus on the **Gaussian + Isotropic + Cut** model. Other models are discussed at the end of this section and in Appendix C.

In Figure 2, we show the posterior predictive distribution (PPD) of black hole spin-orbit tilts. In the left panel, we only show the low-mass Gaussian component ($m_1 \lesssim \tilde{m}$), i.e., we construct quantiles of

$$\pi_G(\cos \theta) = \pi_t(\cos \theta | \mu_{t,k}, \sigma_{t,k}), \quad (7)$$

where $k = 1, 2, \dots$ correspond to individual samples of the posterior obtained with *GWpopulation* (some of which are shown in Figure 2 by thin blue lines). Thus, the PPD is a one-dimensional distribution on the black

hole spin tilts which is obtained by marginalising over the two-dimensional distribution of $\cos\theta_{1(2)}$ in Equation (3). In the right panel, we include the low-mass isotropic component, i.e., we consider

$$\pi_{\text{GI}}(\cos\theta) = \xi_k \pi_t(\cos\theta | \mu_{t,k}, \sigma_{t,k}) + \frac{1 - \xi_k}{2}. \quad (8)$$

The right panel shows excellent agreement with the non-parametric B-Spline model of [The LIGO, Virgo, and KAGRA Collaborations \(2025a,e\)](#) and earlier parametric analyses of [S. Vitale et al. \(2022\)](#), which exhibit a similar peak near $\cos\theta \approx 0$ and lends further credibility to our analysis. The left panel shows that its Gaussian component, which is responsible for the overabundance at near-perpendicular orientations, agrees well with the expected tilt distribution (red) of mergers caused by the Lidov–Kozai effect in triples ([F. Antonini et al. 2018](#)). However, it is in stark contradiction with expectations from traditional isolated binary formation scenario (orange) which peak sharply at $\cos\theta = 1$ ([A. Olejak et al. 2024](#)) even if large natal kicks are considered (dashed). We further discuss the astrophysical implications of our findings in Section 4.

In Appendix B, we show that the PPD of the black hole spin tilt distribution of the low-mass Gaussian component is the result of posterior distributions with a small non-zero mean $\mu_t = 0.20^{+0.21}_{-0.11}$ and standard deviation $\sigma_t = 0.55^{+0.25}_{-0.16}$ which deviate significantly from their priors $\mu_t \sim \mathcal{U}_{[-1,1]}$ and $\sigma_t \sim \mathcal{N}_{[0.1,4]}(\mu = 0, \sigma = 1/2)$, respectively. We also find that the Gaussian component is the dominant component in the low-mass population ($\xi = 0.86^{+0.11}_{-0.54}$) where the small isotropic contribution ($1 - \xi$) causes the vertical shift of the PPD from the left to the right panel of Figure 2. A complete absence of the Gaussian component ($\xi = 0$) is disfavoured but cannot be ruled out with certainty. For the mass threshold that separates the low-mass population from the high-mass isotropic population we infer $\tilde{m} = 44.26^{+8.60}_{-4.56} M_\odot$ which agrees with previous findings ([Y.-Z. Wang et al. 2022](#); [Y.-J. Li et al. 2024](#); [F. Antonini et al. 2025b,a](#); [H. Tong et al. 2025](#); [C. Plunkett et al. 2026](#)).

In Figure 3, we present the PPDs for the spin magnitudes of the low-mass Gaussian component (parametrised by μ_χ and σ_χ), low-mass isotropic component (μ_χ^{Iso} and σ_χ^{Iso}), and high-mass isotropic component ($\mu_\chi^{\text{HighIso}}$ and $\sigma_\chi^{\text{HighIso}}$). The dominant low-mass Gaussian component (blue) tends to have small non-zero spins similar to findings of [The LIGO, Virgo, and KAGRA Collaborations \(2025a\)](#). The subdominant low-mass isotropic component (orange) tends to exhibit somewhat larger spin magnitudes. However, the large uncertainty hinders reliable interpretations. Meanwhile, the high-mass isotropic component (purple) appears to

peak at significantly larger values $\gtrsim 0.5$ which would be expected if those include highly spinning black holes formed through hierarchical mergers ([D. Gerosa & M. Fishbach 2021](#)) or through gas-accretion in active galactic nuclei. We highlight that the mismatches of each component with the non-parametric B-Spline model by the [The LIGO, Virgo, and KAGRA Collaborations \(2025a,e\)](#) is expected as the latter fits for the entire merger population and does not differentiate between subpopulations.

In Appendix C, we present the mixing fractions ξ of the Gaussian component across different models (except **Gaussian** and **Aligned** where no mixing was assumed, cf. Table 1). The **Aligned + Isotropic** and **Aligned + Isotropic + Cut** models show that if alignment was enforced it would only contribute by $\xi = 0.15^{+0.11}_{-0.06}$ and $0.09^{+0.66}_{-0.06}$, respectively, which further disfavours significant contribution from an aligned component. Comparing the **Gaussian + Isotropic** and **Uniform Gaussian + Isotropic** models to their LVK counterparts (which enforce the same spin magnitude distribution in the Gaussian and isotropic components) we observe a peculiar bi-modality around $\xi \approx 0.2$ and 0.8 in the former. However, the peak around 0.2 vanishes if only the mixing within the low-mass population in the **Gaussian + Isotropic + Cut** model is considered, which suggests that it is an artefact of the isotropic high-mass population.

In Appendix C (Figure 10), we also show the PPDs of the spin-orbit tilts and spin magnitudes across all other models than **Gaussian + Isotropic + Cut**. In particular, it shows that models which enforce alignment of the Gaussian component (**Aligned**, **Aligned + Isotropic**, and **Aligned + Isotropic + Cut**) and **Uniform Gaussian + Isotropic** with a uniform prior on σ_t fail to recover the peaked shape of the non-parametric B-Spline model ([The LIGO, Virgo, and KAGRA Collaborations 2025a,e](#)).

4. ASTROPHYSICAL IMPLICATIONS

Most massive progenitor stars of black holes or neutron stars are found in hierarchical triples or higher-order configurations (e.g., [M. Moe & R. Di Stefano 2017](#); [S. S. R. Offner et al. 2023](#)), where a close inner binary is orbited by one or more outer distant companions. The gravitational three-body dynamics of hierarchical triples can naturally lead to binary mergers in which the component spins are preferentially nearly perpendicular to the inner orbital angular momentum ([F. Antonini et al. 2018](#); [C. L. Rodriguez & F. Antonini 2018](#)). [B. Liu & D. Lai \(2018\)](#) showed that this arises because the spin of a black hole in the inner binary evolves through a combi-

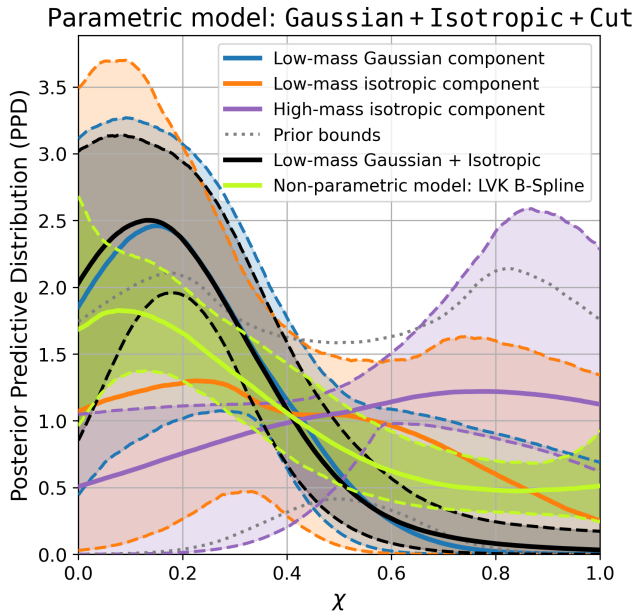


Figure 3. PPD of the black hole spin magnitude distribution in the Gaussian Isotropic Cut model. Blue shows the magnitude distribution of the low-mass Gaussian component (parametrised by μ_χ and σ_χ), orange of the low-mass isotropic component (μ_χ^{iso} and σ_χ^{iso}), and purple of the high-mass isotropic component ($\mu_\chi^{\text{HighIso}}$ and $\sigma_\chi^{\text{HighIso}}$). The transition between low- and high-mass components is inferred at a primary mass cut-off of $\tilde{m} \approx 44.3_{-4.6}^{+8.7} M_\odot$. The green colour shows the non-parametric B-Spline model of The LIGO, Virgo, and KAGRA Collaborations (2025a,e). Solid lines and shaded envelopes indicate medians and 90% credible intervals, respectively. The dotted lines show the prior bounds of the single-component models.

nation of de Sitter precession around the inner orbital angular momentum $\mathbf{L} \equiv \mathbf{L}_{\text{in}}$, the precession of \mathbf{L}_{in} itself around the outer orbital axis \mathbf{L}_{out} , and the gradual shrinking of the inner binary orbit due to gravitational-wave energy-loss.

The evolution of the spin can be described by the precession equation $d\chi/dt = \boldsymbol{\Omega}_p \times \boldsymbol{\chi}$, where the effective precession (rotation) vector is given by $\boldsymbol{\Omega}_p = \Omega_L \hat{\mathbf{L}}_{\text{out}} + \Omega_{\text{SL}} \hat{\mathbf{L}}_{\text{in}}$. Here, Ω_L and Ω_{SL} denote the precession rates associated with the orbital motion of the inner binary around the tertiary and the de Sitter spin-orbit coupling, respectively. The direction of $\boldsymbol{\Omega}_p$ defines the instantaneous precession axis of the spins.

In the adiabatic regime, where the evolution of $\boldsymbol{\Omega}_p$ is slow compared to the spin precession rate, the quantity $\cos \bar{\theta}_p = \hat{\boldsymbol{\chi}} \cdot \hat{\boldsymbol{\Omega}}_p$ is nearly conserved, implying that the angle between the spin vector and the precession axis remains approximately constant. At large separations, $\boldsymbol{\Omega}_p$ is dominated by the outer orbital term, such that $\boldsymbol{\Omega}_p \simeq \Omega_L \hat{\mathbf{L}}_{\text{out}}$. If the component spins are initially

aligned with \mathbf{L}_{in} , and \mathbf{L}_{in} is inclined close to 90° relative to \mathbf{L}_{out} as required for Lidov–Kozai mergers, the spins are initially nearly perpendicular to $\boldsymbol{\Omega}_p$ (i.e. $\theta_p \approx 90^\circ$).

As the tertiary companion drives the inner binary to large eccentricities where efficient gravitational-wave emission at close pericentre passages shrinks the inner orbit, the coupling to the tertiary weakens, and Ω_{SL} gradually overtakes Ω_L , causing $\hat{\boldsymbol{\Omega}}_p$ to transition smoothly from being aligned with \mathbf{L}_{out} to being aligned with \mathbf{L}_{in} . Because θ_p is an adiabatic invariant, the spin maintains its inclination of $\simeq 90^\circ$ relative to the evolving precession axis. By the time the system decouples and the inner binary merges, the component spins therefore lie nearly within the orbital plane, leading to small values of χ_{eff} but potentially large in-plane spin components. Meanwhile, the angles between the two spins in the orbital plane of the binary may be distributed across the whole range between 0 and 180° due to generally different spin precession rates of the black holes if $m_1 \neq m_2$ (C. L. Rodriguez & F. Antonini 2018, see Figure 10 therein).

In contrast, binary black hole mergers formed through the evolution of isolated binary stars are generally expected to have spins closely aligned with the orbital angular momentum, resulting in low misalignment angles and a preference for positive effective spins (V. Kalogera 2000; W. M. Farr et al. 2017; D. Gerosa et al. 2018; K. Belczynski et al. 2020; S. S. Bavera et al. 2020; A. Olejak & K. Belczynski 2021; F. S. Broekgaarden et al. 2022). In standard binary-evolution models, stellar spins are assumed to be aligned with the orbital angular momentum prior to core collapse, and any natal kick imparted during the collapse tilts the orbital plane, thereby directly setting the resulting spin-orbit misalignment (e.g., N. Brandt & P. Podsiadlowski 1995; V. Kalogera 2000; T. Fragos et al. 2010; T. M. Tauris et al. 2017), with the maximum tilt limited by the risk to disrupt the binary. As exemplified in Figure 2, even under the assumption of very high black hole natal kicks—which are not expected for massive black holes from an evolutionary perspective (H. T. Janka & D. Kresse 2024)—the resulting distribution remains strongly peaked at modest tilt angles, corresponding to $\cos \theta \gtrsim 0.75$.

Producing a distribution with a significant fraction of systems at $\cos \theta \lesssim 0.75$ via isolated binary channels requires non-standard and poorly constrained assumptions, such as highly misaligned progenitor spins, “spin tossing” at black hole formation (T. M. Tauris 2022), or finely tuned correlations between spin orientations and natal-kick directions (V. Baibhav & V. Kalogera 2024). In particular, reproducing an observed peak near $\cos \theta \approx 0$ would require preferentially orienting black

hole spins perpendicular to the natal kicks (V. Baibhav & V. Kalogera 2024, see Figure 5 therein). Such an assumption is highly non-standard and is challenged by observational constraints from, e.g., pulsars’ velocity-spin alignment (S. Johnston et al. 2005; A. Noutsos et al. 2012, 2013; I. Mandel & A. P. Igoshev 2023) as well as by simulation results of core-collapse supernovae (e.g., A. Burrows et al. 2024).

Another possibility discussed in the literature is a spin flip induced by mass transfer (J. Stegmann & F. Antonini 2021), which could produce in-plane tilts. This mechanism could reduce the first-born black hole’s spin projection onto the orbital angular momentum; however, its nature and efficiency remain highly uncertain as it requires very efficient angular momentum transport between the stellar core and envelope and inefficient tides which would otherwise realign the spins after mass transfer.

Alternatively, S. Vitale & M. Mould (2025) discuss the possibility that parametric modelling for an underlying preferentially aligned merger population may lead to inference of spurious peaks away from perfect alignment due to measurement uncertainties and the finiteness of the current sample size. This highlights that it is essential to verify the non-parametric inference of The LIGO, Virgo, and KAGRA Collaborations (2025a) and our parametric analysis with the growing gravitational-wave dataset in the future. However, we stress that S. Vitale & M. Mould (2025) tested underlying preferentially aligned populations ($\mu_t = 1$) which are extremely broad with $\sigma_t = 1.15$, which seems inconsistent with current expectations from astrophysical models that tend to be narrower (see Section 2). Even in that case, their spurious peaks away from alignment are not as narrowly peaked as close to $\cos\theta \approx 0$ as the feature in the GWTC-4.0 data.

5. SUMMARY AND DISCUSSION

The latest gravitational-wave data GWTC-4.0 has enabled The LIGO, Virgo, and KAGRA Collaborations (2025a) to infer a global peak near $\cos\theta \approx 0$ in non-parametric models for the spin-orbit tilt angle distribution of the binary black hole merger population. In this work, we have recovered this distribution with parametric models that contain a dominant pronounced Gaussian peak at near-perpendicular directions. This defies traditional formation scenarios from isolated massive binary stars, which recover significant spin-orbit misalignment only under fine-tuned or highly uncertain assumptions of the binary evolution and stellar collapse (Section 4). Instead, the latest gravitational-wave data suggests an alternative explanation for the main origin of

binary black hole mergers, which builds upon the fact that most massive black hole progenitor stars are found in hierarchical triple or higher-order configurations (M. Moe & R. Di Stefano 2017; S. S. R. Offner et al. 2023). In these systems, the relativistic gravitational dynamics of three-body systems naturally produces mergers with near-perpendicular spin angles (F. Antonini et al. 2018; B. Liu & D. Lai 2018), while they could also yield event rates (I. Mandel & F. S. Broekgaarden 2022, and references therein) which are broadly consistent with gravitational-wave observations (The LIGO, Virgo, and KAGRA Collaborations 2025a). Triples have also been shown to be in overall agreement with key features of the observationally inferred mass distributions such as a global peak at $\sim 10 M_\odot$ and declining rate towards higher masses (e.g., F. Antonini et al. 2017; K. Silsbee & S. Tremaine 2017; J. Stegmann et al. 2022a,b). However, we note that there are no comprehensive studies that investigate the impact of assumptions in the stellar evolution (e.g., inner binary mass transfer or natal kicks) and account for delay time distribution and metallicity-dependent star-formation history, which are needed for robust comparison to gravitational-wave data.

We highlight that the spin distribution from triples also agrees qualitatively well with the inferred distribution of χ_{eff} , which is skewed and asymmetric about zero with more support for positive values (The LIGO, Virgo, and KAGRA Collaborations 2025a; S. Banagiri et al. 2025). Due to the natural preference to produce tilts at $\cos\theta \approx 0$ similar χ_{eff} distributions have been obtained for triples, largely independent of the assumed spin magnitudes (e.g., C. L. Rodriguez & F. Antonini 2018, see Figure 9 therein). In addition, a triple formation scenario could contribute to the growing number of claims about mergers with residual orbital eccentricity (I. Romero-Shaw et al. 2022; N. Gupte et al. 2024; H. L. Iglesias et al. 2024; M. de Lluc Planas et al. 2025; G. Morras et al. 2025; K. S. Phukon et al. 2025), which would be impossible to recover from isolated binary star evolution (e.g., K. Belczynski et al. 2002; G. Fumagalli et al. 2024). While some of the eccentric binary black hole candidates have masses that are confidently within the upper mass gap and may only plausibly explained by hierarchical mergers in dense environments (e.g., I. Romero-Shaw et al. 2020; V. Gayathri et al. 2020), candidates below the upper mass could be also explained by the Lidov–Kozai triples mechanism (I. Romero-Shaw et al. 2025b; P. McMillin et al. 2025), where the subset of non-adiabatic triples is expected to yield a small fraction of eccentric outlier detections (e.g., F. Antonini et al. 2017; C. L. Rodriguez & F. Antonini 2018; B. Liu et al. 2019). In particular, it has been argued that re-

cent claims for residual eccentricity in one neutron star-black hole (NSBH) merger (G. Morras et al. 2025; M. de Lluc Planas et al. 2025; K. Kacanja et al. 2025; A. Jan et al. 2025) may only be obtained through triple star evolution (J. Stegmann & J. Klencki 2025) and imply a dominant contribution to the total NSBH merger rate (I. Romero-Shaw et al. 2025a).

If black hole mergers indeed tend to result from triple rather than binary star evolution, it would suggest that binary mass transfer is less efficient in forming very close binary black hole systems than previously assumed, e.g., in scenarios involving successful common envelope ejection (K. Belczynski et al. 2020). This may indicate that binary black hole progenitors instead tend to undergo stable mass transfer (M. Gallegos-Garcia et al. 2021), which typically produces systems with wider orbital separations than those expected from a common envelope scenario (S. S. Bavera et al. 2020; A. Olejak et al. 2021; L. A. C. van Son et al. 2022). Moreover, recent studies have predicted that the minimum separation of binary black hole systems formed via binary evolution may be limited by a delayed unstable mass transfer and stellar mergers (J. Klencki et al. 2025). Also, observations of other types of binaries hosting compact objects fur-

ther challenge standard binary evolution models. Notable examples are Gaia black holes (K. El-Badry et al. 2023a; S. Chakrabarti et al. 2023; K. El-Badry et al. 2023b), whose properties cannot be reconciled with conventional models (P. Nagarajan et al. 2025) and likely require non-standard assumptions about angular momentum loss during mass transfer (A. Olejak et al. 2025).

ACKNOWLEDGMENTS

We thank the two anonymous reviewers, Colm Talbot, Isobel Romero-Shaw, and Carlos Lousto for useful comments and input that helped improving this work. FA and VR are supported by the UK’s Science and Technology Facilities Council grants ST/V005618/1 and UKRI2489. S.R. is funded by the Deutsche Forschungsgemeinschaft (DFG, German Research Foundation) – project number 546677095. This material is based upon work supported by NSF’s LIGO Laboratory which is a major facility fully funded by the National Science Foundation.

Software: `GWpopulation` (C. Talbot et al. 2019; C. Talbot et al. 2025); `Bilby` (G. Ashton et al. 2019); `GWpopulation Pipe` (C. Talbot 2021)

APPENDIX

A. MASS AND REDSHIFT MODELLING

In all our models, we assume a simple parameterisation of our mass distribution as (C. Talbot et al. 2019; C. Talbot et al. 2025)

$$\pi(m_1, q) = \pi(m_1)\pi(q|m_1), \quad (\text{A1})$$

where $0 < q \leq 1$ is the binary mass ratio and

$$\pi(m_1) = (1 - \lambda_m)\pi_{\text{pow}}(m_1) + \lambda_m\pi_{\text{norm}}(m_1), \quad (\text{A2})$$

$$\pi_{\text{pow}}(m_1) \propto m^{-\alpha} \quad \text{with} \quad m_{\text{min}} \leq m_1 < m_{\text{max}}, \quad (\text{A3})$$

$$\pi_{\text{norm}}(m_1) \propto \exp\left(-\frac{(m_1 - \mu_m)^2}{2\sigma_m^2}\right) \quad \text{with} \quad m_{\text{min}} \leq m_1 < 100 M_{\odot}, \quad (\text{A4})$$

$$\pi(q|m_1) = \frac{1 + \beta}{1 - (m_{\text{min}}/m_1)^{1+\beta}} q^{\beta}. \quad (\text{A5})$$

Thus, the primary mass distribution is modelled as a power-law with a Gaussian component and the conditional mass-ratio distribution as a power-law.

For the distribution in redshift z we assume a power-law following M. Fishbach et al. (2018)

$$\pi(z) = (1 + z)^{\lambda}. \quad (\text{A6})$$

Parameter	Description	Prior
λ_m	m_1 mixture fraction	$\mathcal{U}_{[0,1]}$
α	m_1 power-law index	$\mathcal{U}_{[-2,4]}$
m_{min}/M_{\odot}	minimum mass	$\mathcal{U}_{[2.0,2.5]}$
m_{max}/M_{\odot}	maximum mass	$\mathcal{U}_{[80,100]}$
μ_m/M_{\odot}	m_1 Gaussian component peak	$\mathcal{U}_{[10,50]}$
σ_m/M_{\odot}	m_1 Gaussian component width	$\mathcal{U}_{[1,10]}$
β	mass ratio power-law index	$\mathcal{U}_{[-4,12]}$
λ	redshift power-law index	$\mathcal{U}_{[-1,10]}$

Table 2. Prior distributions for mass and redshift model hyper-parameters.

For all hyper-parameters introduced in Equations (A2) – (A6) we assume uniform priors within the bounds given in Table 2 (C. Talbot et al. 2019; C. Talbot et al. 2025).

We emphasise that for models that mix two components (3 – 9 in Table 1) we assume the *same* mass and redshift modelling for both, which is consistent with the approach of the LVK collaborations (e.g., The LIGO, Virgo, and KAGRA Collaborations 2023b, 2025a). However, if both components represent two different astrophysical formation channels (e.g., a near-

perpendicular Gaussian from triple star evolution and an isotropic component from dynamical interactions in star clusters) they could in reality follow different mass and redshift distributions (cf., [A. Dorozsmai et al. 2025](#)). Investigating the impact of our simplification as well as allowing for any spin correlation with mass or redshift are left for future work.

B. SUPPLEMENTARY RESULTS ABOUT THE GAUSSIAN + ISOTROPIC + CUT MODEL

In [Figure 4](#) we show a corner plot of all hyper-parameters of the **Gaussian + Isotropic + Cut** model. Regarding the spin properties, it shows that the near-perpendicular Gaussian component ($\mu_t = 0.20_{-0.11}^{+0.21}$ and $\sigma_t = 0.55_{-0.16}^{+0.25}$) is the dominant component ($\xi = 0.86_{-0.54}^{+0.11}$) at low masses ($m_1 \lesssim \tilde{m} = 44.26_{-4.56}^{+8.60} M_\odot$). In addition, [Figure 5](#) displays that the PPD of the $\zeta(m_1, \tilde{m})$ for posterior draws of \tilde{m} , showing that the transition is significantly different from the prior draws. Moreover, [Figure 6](#) shows the corner plot of all hyper-parameters if \tilde{k} in [Equation \(4\)](#) is treated as a free parameter (see [Section 2](#)). Comparison to [Figure 4](#) shows that the posterior distribution of all other parameters remain largely similar. We also find that the **Gaussian + Isotropic + Cut** model remains preferred over **Aligned + Isotropic + Cut** model if \tilde{k} is treated as a free parameter in both cases with $\Delta \ln \mathcal{B} = -2.5$.

C. OTHER POPULATION MODELS

[Figure 7](#) shows the marginal posterior distributions of the Gaussian mixing fraction ξ . In all models, where the Gaussian is allowed to move freely ($-1 \leq \mu_t \leq 1$) it dominates the distribution, while allowing for a potential mixing with a subdominant isotropic component. Enforcing a preferentially aligned spin-orbit configuration ($\mu_t = 1$ in **Aligned + Isotropic** and **Aligned + Isotropic + Cut**) makes the Gaussian component a subdominant contribution, suggesting no preference for alignment in the gravitational-wave data. [Figure 7](#) shows only small probabilities for the aligned components to be dominant, e.g., the cumulative density function yields $P(\xi \lesssim 0.8) \approx 0.95$ and 0.85 in the **Aligned + Isotropic** and **Aligned + Isotropic + Cut** models, respectively. However, [Figure 8](#) shows that a large aligned contribution $\xi \lesssim 1$ is correlated with large width $\sigma_t \approx 1$ (which is different to the **Gaussian + Isotropic + Cut** model in [Figure 4](#)). Thus, we conclude that the Bayes factors disfavour aligned models at varying degree (see [Section 3](#)) and even if realised they are either a subdominant component ([Figure 7](#)) or they dominate but are too wide to be plausibly explained by isolated

binary formation scenarios (see [Section 4](#)) and indistinguishable from the isotropic component (see [Figure 10](#) below).

In [Figure 9](#), we further investigate the preference against an aligned component. We explore variants where the aligned component is restricted to $\cos \theta \in [t_{\min}, 1]$ for some fixed threshold value t_{\min} , since realistic isolated binary evolution scenarios may yield spin-orbit tilts which are more narrowly confined than the entire range $\cos \theta \in [-1, 1]$. For this purpose, we follow a similar approach to [T. A. Callister et al. \(2022\)](#); [H. Tong et al. \(2022\)](#) and adopt the **Aligned + Isotropic + Cut** model but use truncated normal distributions $\mathcal{N}_{[t_{\min}, 1]}(\cos \theta_i | \mu_t = 1, \sigma_t)$ in [Equation \(2\)](#) with $t_{\min} = -1.0, -0.9, -0.8, \dots, 0.9$. The left panel of [Figure 9](#) shows that larger values of t_{\min} (i.e., more narrowly distributed spin-orbit angles about alignment) require smaller contributions from the aligned component, ranging from $\xi(t_{\min} = -1) = 0.09_{-0.06}^{+0.66}$ to $\xi(t_{\min} = 0.9) = 0.01 \pm 0.01$. In the right panel, we compare the modified **Aligned + Isotropic + Cut** models to the **Gaussian + Isotropic + Cut** model (where the Gaussian component remains confined to $\cos \theta \in [-1, 1]$). Evidence against the aligned models is positive ([R. E. Kass & A. E. Raftery 1995](#)) with $|\Delta \ln \mathcal{B}| \approx 1$ to 3 across the whole range of t_{\min} . We also might see a tendency that above $t_{\min} \gtrsim 0.3$ models become more strongly disfavoured, which would also roughly coincide with the depletion of spin-orbit tilt angles in the non-parametric B-Spline model (cf. [Figure 2](#)). However, we do note that the scatter in $\Delta \ln \mathcal{B}$ across different explored models is rather large and inhibits definite conclusions. Since $\Delta \ln \mathcal{B}$ scales roughly with the detected sample size ([R. E. Kass & A. E. Raftery 1995](#)) we expect the robustness of the model comparison to improve soon as the gravitational-wave catalogue grows during the fourth and fifth, as well as a possible intermediate, LVK observing runs.

In addition, [Figure 10](#) shows that the PPD of the spin-orbit tilts in most models with a free Gaussian recover the pronounced peak at $\cos \theta \approx 0$ of the non-parametric model ([The LIGO, Virgo, and KAGRA Collaborations 2025a](#)). The peak is less pronounced and recovered in models that assume a uniform prior on σ_t (**Uniform Gaussian + Isotropic** and **LVK Uniform Gaussian + Isotropic**), where shallow distributions with large values of σ_t mimic an isotropic distribution. As discussed in [Section 2](#), a uniform prior on σ_t is not expected from astrophysical source modelling. We note that **LVK Uniform Gaussian + Isotropic** is a similar to the **Gaussian + Isotropic** model by [The LIGO,](#)

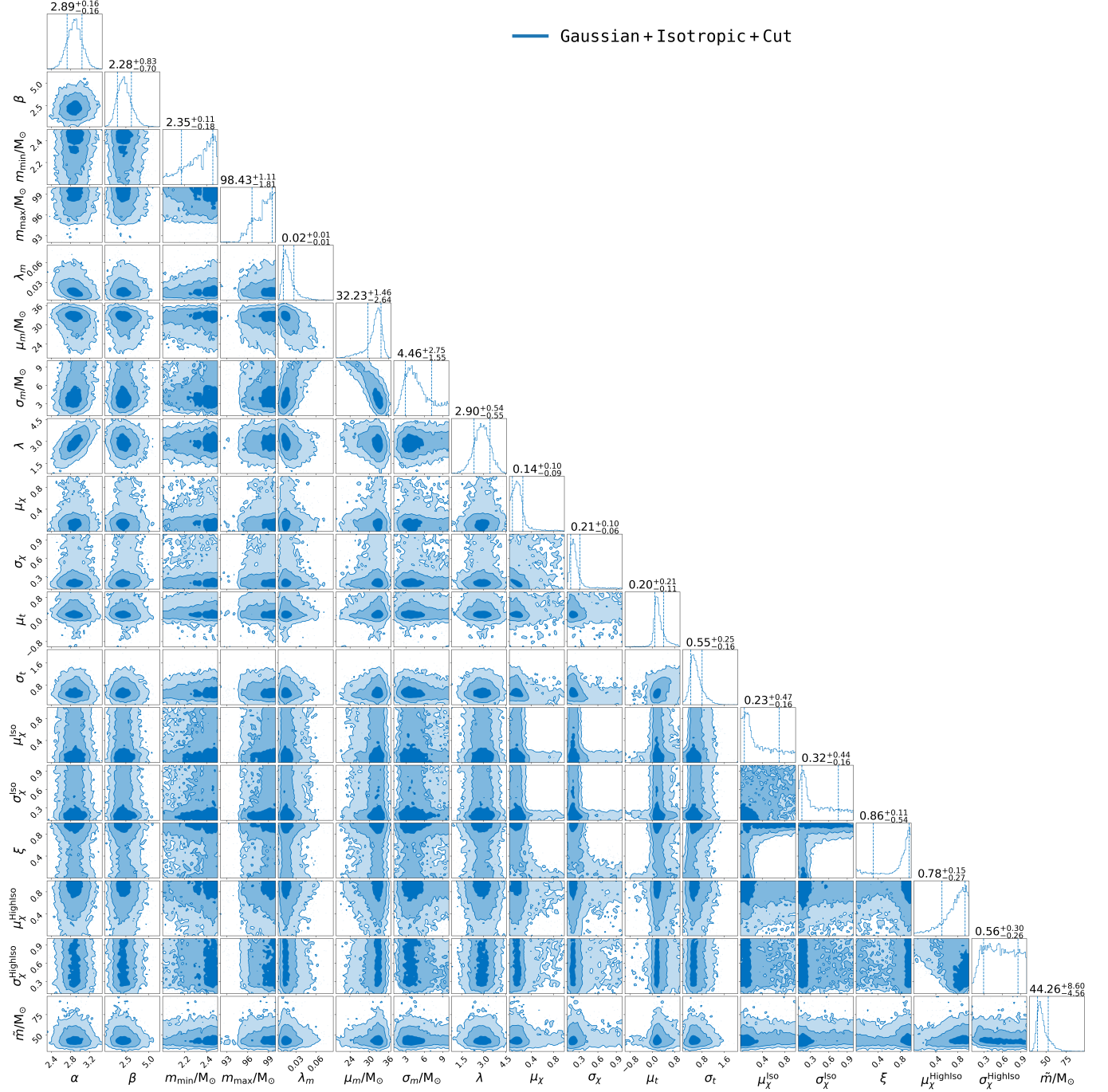


Figure 4. All joint and marginal posteriors in the Gaussian + Isotropic + Cut model. Variables are defined in Section 2 and Appendix A.

Virgo, and KAGRA Collaborations (2025a) and recovers a similar PPD.

REFERENCES

Aasi, J., Abbott, B. P., Abbott, R., et al. 2015, *Classical and Quantum Gravity*, 32, 074001, doi: 10.1088/0264-9381/32/7/074001

Abbott, B. P., Abbott, R., Abbott, T. D., et al. 2016, *PhRvL*, 116, 061102, doi: 10.1103/PhysRevLett.116.061102

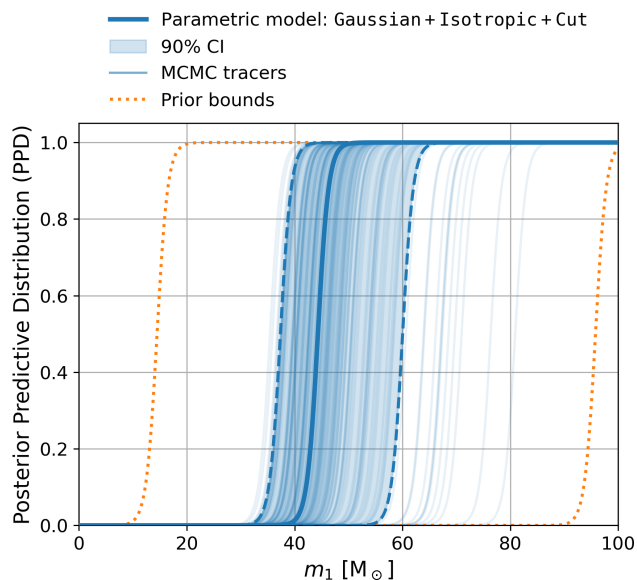


Figure 5. PPD of the cut-off Equation (4) in the **Gaussian + Isotropic + Cut** model. Blue shows the PPD for posterior draws of \tilde{m} , and orange shows the 90% bounds for prior draws of \tilde{m} (uniform distribution $\mathcal{U}_{[10 M_{\odot}, 100 M_{\odot}]}$, see Section 2).

- Abbott, B. P., Abbott, R., Abbott, T. D., et al. 2018, *Living Reviews in Relativity*, 21, 3, doi: [10.1007/s41114-018-0012-9](https://doi.org/10.1007/s41114-018-0012-9)
- Acernese, F., Agathos, M., Agatsuma, K., et al. 2015, *Classical and Quantum Gravity*, 32, 024001, doi: [10.1088/0264-9381/32/2/024001](https://doi.org/10.1088/0264-9381/32/2/024001)
- Akutsu, T., Ando, M., Arai, K., et al. 2020, *Progress of Theoretical and Experimental Physics*, 2021, 05A101, doi: [10.1093/ptep/ptaa125](https://doi.org/10.1093/ptep/ptaa125)
- Antonini, F., Rodriguez, C. L., Petrovich, C., & Fischer, C. L. 2018, *Mon. Not. R. Astron. Soc.*, 480, L58, doi: [10.1093/mnrasl/sly126](https://doi.org/10.1093/mnrasl/sly126)
- Antonini, F., Romero-Shaw, I., Callister, T., et al. 2025a, *arXiv e-prints*, arXiv:2509.04637, doi: [10.48550/arXiv.2509.04637](https://doi.org/10.48550/arXiv.2509.04637)
- Antonini, F., Romero-Shaw, I. M., & Callister, T. 2025b, *PhRvL*, 134, 011401, doi: [10.1103/PhysRevLett.134.011401](https://doi.org/10.1103/PhysRevLett.134.011401)
- Antonini, F., Toonen, S., & Hamers, A. S. 2017, *Astrophys. J.*, 841, 77, doi: [10.3847/1538-4357/aa6f5e](https://doi.org/10.3847/1538-4357/aa6f5e)
- Ashton, G., Hübner, M., Lasky, P. D., et al. 2019, *ApJS*, 241, 27, doi: [10.3847/1538-4365/ab06fc](https://doi.org/10.3847/1538-4365/ab06fc)
- Aso, Y., Michimura, Y., Somiya, K., et al. 2013, *PhRvD*, 88, 043007, doi: [10.1103/PhysRevD.88.043007](https://doi.org/10.1103/PhysRevD.88.043007)
- Baibhav, V., & Kalogera, V. 2024, . <https://arxiv.org/abs/2412.03461>
- Banagiri, S., Callister, T. A., Adamcewicz, C., Doctor, Z., & Kalogera, V. 2025, *ApJ*, 990, 147, doi: [10.3847/1538-4357/adf4c6](https://doi.org/10.3847/1538-4357/adf4c6)
- Bavera, S. S., Fragos, T., Qin, Y., et al. 2020, *A&A*, 635, A97, doi: [10.1051/0004-6361/201936204](https://doi.org/10.1051/0004-6361/201936204)
- Belczynski, K., Kalogera, V., & Bulik, T. 2002, *Astrophys. J.*, 572, 407, doi: [10.1086/340304](https://doi.org/10.1086/340304)
- Belczynski, K., Repetto, S., Holz, D. E., et al. 2016, *Astrophys. J.*, 819, 108, doi: [10.3847/0004-637X/819/2/108](https://doi.org/10.3847/0004-637X/819/2/108)
- Belczynski, K., Klencki, J., Fields, C. E., et al. 2020, *A&A*, 636, A104, doi: [10.1051/0004-6361/201936528](https://doi.org/10.1051/0004-6361/201936528)
- Biscoveanu, S., Isi, M., Varma, V., & Vitale, S. 2021, *PhRvD*, 104, 103018, doi: [10.1103/PhysRevD.104.103018](https://doi.org/10.1103/PhysRevD.104.103018)
- Brandt, N., & Podsiadlowski, P. 1995, *MNRAS*, 274, 461, doi: [10.1093/mnras/274.2.461](https://doi.org/10.1093/mnras/274.2.461)
- Broekgaarden, F. S., Berger, E., Stevenson, S., et al. 2022, *Mon. Not. R. Astron. Soc.*, 516, 5737, doi: [10.1093/mnras/stac1677](https://doi.org/10.1093/mnras/stac1677)
- Burrows, A., Wang, T., Vartanyan, D., & Coleman, M. S. B. 2024, *Astrophys. J.*, 963, 63, doi: [10.3847/1538-4357/ad2353](https://doi.org/10.3847/1538-4357/ad2353)
- Callister, T. A., Miller, S. J., Chatziioannou, K., & Farr, W. M. 2022, *ApJL*, 937, L13, doi: [10.3847/2041-8213/ac847e](https://doi.org/10.3847/2041-8213/ac847e)
- Chakrabarti, S., Simon, J. D., Craig, P. A., et al. 2023, *AJ*, 166, 6, doi: [10.3847/1538-3881/accc21](https://doi.org/10.3847/1538-3881/accc21)
- Colleoni, M., Ramis Vidal, F. A., García-Quirós, C., Akçay, S., & Bera, S. 2025, *PhRvD*, 111, 104019, doi: [10.1103/PhysRevD.111.104019](https://doi.org/10.1103/PhysRevD.111.104019)
- Damour, T. 2001, *Phys. Rev. D*, 64, 124013, doi: [10.1103/PhysRevD.64.124013](https://doi.org/10.1103/PhysRevD.64.124013)
- de Lluç Planas, M., Husa, S., Ramos-Buades, A., & Valencia, J. 2025, *First eccentric inspiral-merger-ringdown analysis of neutron star-black hole mergers*, <https://arxiv.org/abs/2506.01760>
- de Lluç Planas, M., Ramos-Buades, A., García-Quirós, C., et al. 2025, . <https://arxiv.org/abs/2504.15833>
- Dorozzmai, A., Romero-Shaw, I. M., Vijaykumar, A., et al. 2025, *MNRAS*, doi: [10.1093/mnras/staf1938](https://doi.org/10.1093/mnras/staf1938)
- Edelman, B., Farr, B., & Doctor, Z. 2023, *ApJ*, 946, 16, doi: [10.3847/1538-4357/acb5ed](https://doi.org/10.3847/1538-4357/acb5ed)
- El-Badry, K., Rix, H.-W., Quataert, E., et al. 2023a, *MNRAS*, 518, 1057, doi: [10.1093/mnras/stac3140](https://doi.org/10.1093/mnras/stac3140)
- El-Badry, K., Rix, H.-W., Cendes, Y., et al. 2023b, *MNRAS*, 521, 4323, doi: [10.1093/mnras/stad799](https://doi.org/10.1093/mnras/stad799)
- Essick, R., Coughlin, M. W., Zevin, M., et al. 2025, *PhRvD*, 112, 102001, doi: [10.1103/44x3-hv3y](https://doi.org/10.1103/44x3-hv3y)
- Farr, W. M., Stevenson, S., Miller, M. C., et al. 2017, *Nature*, 548, 426, doi: [10.1038/nature23453](https://doi.org/10.1038/nature23453)

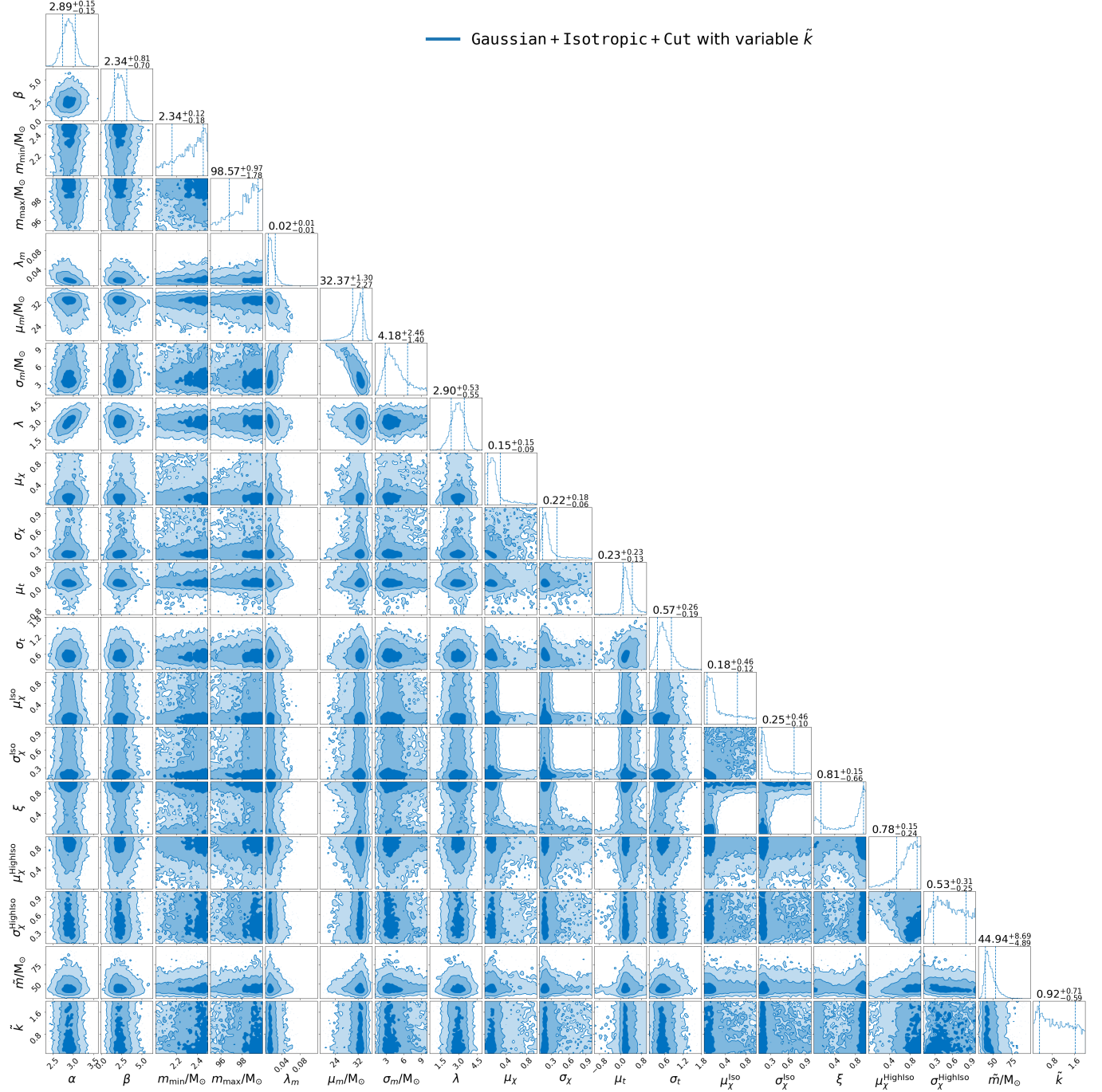


Figure 6. Same as Figure 4 with a free parameter \tilde{k} .

Fishbach, M., Holz, D. E., & Farr, W. M. 2018, *ApJL*, 863, L41, doi: [10.3847/2041-8213/aad800](https://doi.org/10.3847/2041-8213/aad800)

Fragos, T., Tremmel, M., Rantsiou, E., & Belczynski, K. 2010, *ApJL*, 719, L79, doi: [10.1088/2041-8205/719/1/L79](https://doi.org/10.1088/2041-8205/719/1/L79)

Fryer, C. L., Belczynski, K., Wiktorowicz, G., et al. 2012, *ApJ*, 749, 91, doi: [10.1088/0004-637X/749/1/91](https://doi.org/10.1088/0004-637X/749/1/91)

Fumagalli, G., Romero-Shaw, I., Gerosa, D., et al. 2024, *PhRvD*, 110, 063012, doi: [10.1103/PhysRevD.110.063012](https://doi.org/10.1103/PhysRevD.110.063012)

Gallegos-Garcia, M., Berry, C. P. L., Marchant, P., & Kalogera, V. 2021, *Astrophys. J.*, 922, 110, doi: [10.3847/1538-4357/ac2610](https://doi.org/10.3847/1538-4357/ac2610)

Gayathri, V., Healy, J., Lange, J., et al. 2020, arXiv e-prints, arXiv:2009.05461, doi: [10.48550/arXiv.2009.05461](https://doi.org/10.48550/arXiv.2009.05461)

Gerosa, D., Berti, E., O’Shaughnessy, R., et al. 2018, *Phys. Rev. D*, 98, 084036, doi: [10.1103/PhysRevD.98.084036](https://doi.org/10.1103/PhysRevD.98.084036)

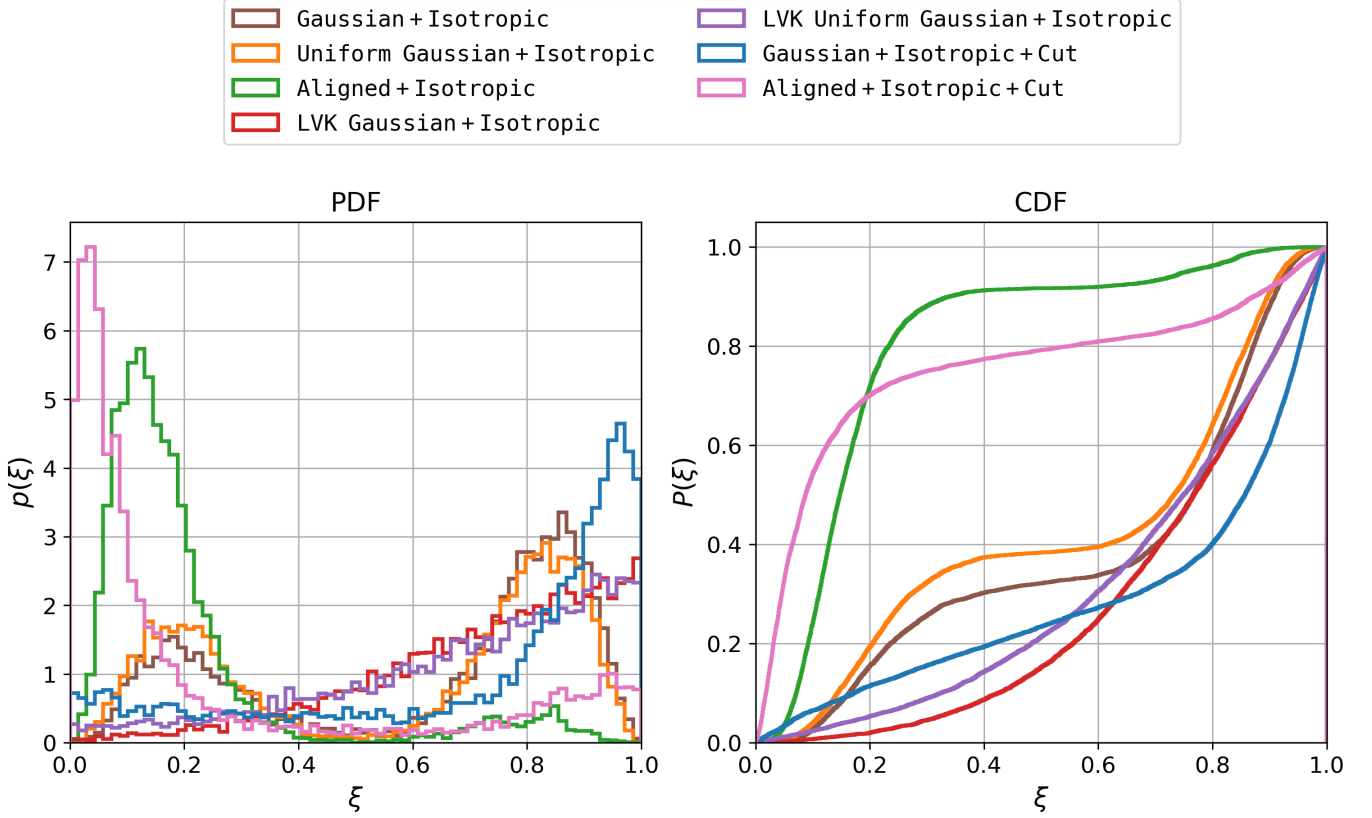


Figure 7. Marginal posterior distributions of the Gaussian mixing fraction ξ . The left panel shows the probability density function (PDF); the right panels its cumulative density function (CDF). The fraction ξ refers to the mixing fraction of the Gaussian component, which is enforced at alignment in the **Aligned + Isotropic** model ($\mu_t = 1$) or moves freely in all others ($-1 \leq \mu_t \leq 1$), whereas $1 - \xi$ refers to the isotropic fraction. For the **Gaussian + Isotropic + Cut** and **Aligned + Isotropic + Cut** models the fractions ξ and $1 - \xi$ describe the mixing in the low-mass population ($m_1 \lesssim \tilde{m}$).

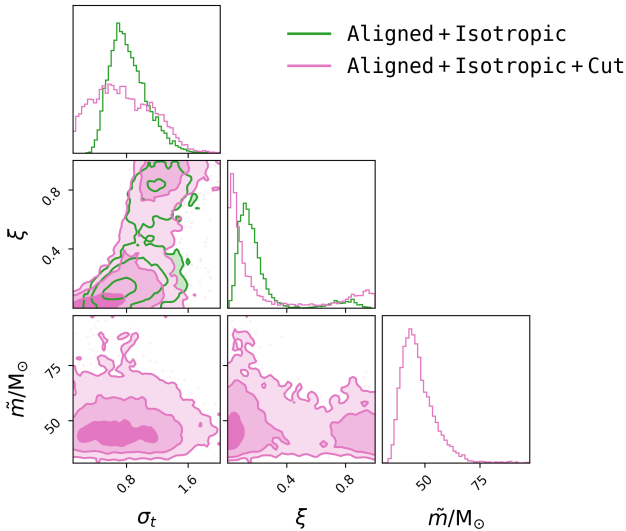


Figure 8. Joint and marginal posteriors for the standard deviation σ_t of the aligned component ($\mu_t = 1$) and its mixing fraction ξ in the **Aligned + Isotropic** model (green) as well as the mass cut-off \tilde{m} in the **Aligned + Isotropic + Cut** model (pink).

- Gerosa, D., & Fishbach, M. 2021, *Nature Astronomy*, 5, 749, doi: [10.1038/s41550-021-01398-w](https://doi.org/10.1038/s41550-021-01398-w)
- Golomb, J., & Talbot, C. 2023, *PhRvD*, 108, 103009, doi: [10.1103/PhysRevD.108.103009](https://doi.org/10.1103/PhysRevD.108.103009)
- Grishin, E., Perets, H. B., & Fragione, G. 2018, *Mon. Not. R. Astron. Soc.*, 481, 4907, doi: [10.1093/mnras/sty2477](https://doi.org/10.1093/mnras/sty2477)
- Gupte, N., Ramos-Buades, A., Buonanno, A., et al. 2024, . <https://arxiv.org/abs/2404.14286>
- Iglesias, H. L., Lange, J., Bartos, I., et al. 2024, *Astrophys. J.*, 972, 65, doi: [10.3847/1538-4357/ad5ff6](https://doi.org/10.3847/1538-4357/ad5ff6)
- Jan, A., Tsao, B.-J., O’Shaughnessy, R., Shoemaker, D., & Laguna, P. 2025, arXiv e-prints, arXiv:2508.12460, doi: [10.48550/arXiv.2508.12460](https://doi.org/10.48550/arXiv.2508.12460)
- Janka, H. T., & Kresse, D. 2024, . <https://arxiv.org/abs/2401.13817>
- Jeffreys, H. 1939, *Theory of Probability*
- Johnston, S., Hobbs, G., Vigeland, S., et al. 2005, *MNRAS*, 364, 1397, doi: [10.1111/j.1365-2966.2005.09669.x](https://doi.org/10.1111/j.1365-2966.2005.09669.x)
- Kacanja, K., Soni, K., & Nitz, A. H. 2025, arXiv e-prints, arXiv:2508.00179, doi: [10.48550/arXiv.2508.00179](https://doi.org/10.48550/arXiv.2508.00179)
- Kalogera, V. 2000, *ApJ*, 541, 319, doi: [10.1086/309400](https://doi.org/10.1086/309400)

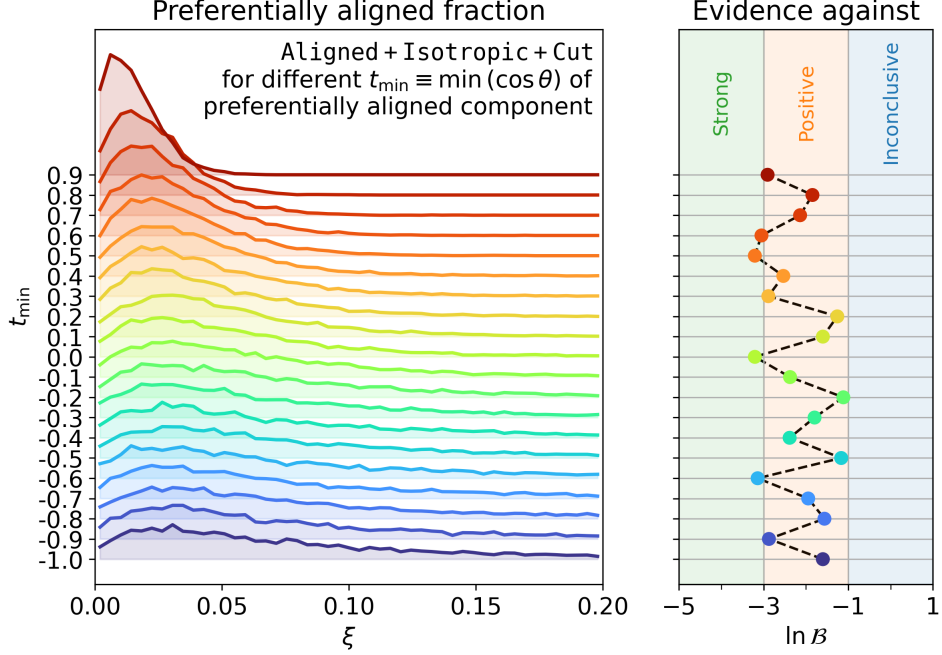


Figure 9. Aligned + Isotropic + Cut model for different lower bounds on $\cos\theta_i$ of the aligned component, i.e., $\mathcal{N}_{[t_{\min}, 1]}(\cos\theta_i | \mu_t = 1, \sigma_t)$ in Equation (2) with $t_{\min} = -1.0, -0.9, -0.8, \dots, 0.9$. The left panel shows the marginal posterior distribution of the contribution ξ of the low-mass aligned component (whereas $1 - \xi$ corresponds to the low-mass isotropic component). The right panel shows the strength of evidence against each aligned model compared to our default **Gaussian + Isotropic + Cut** model, which allows but does not enforce preferentially aligned mergers. Nomenclature follows [R. E. Kass & A. E. Raftery \(1995\)](#).

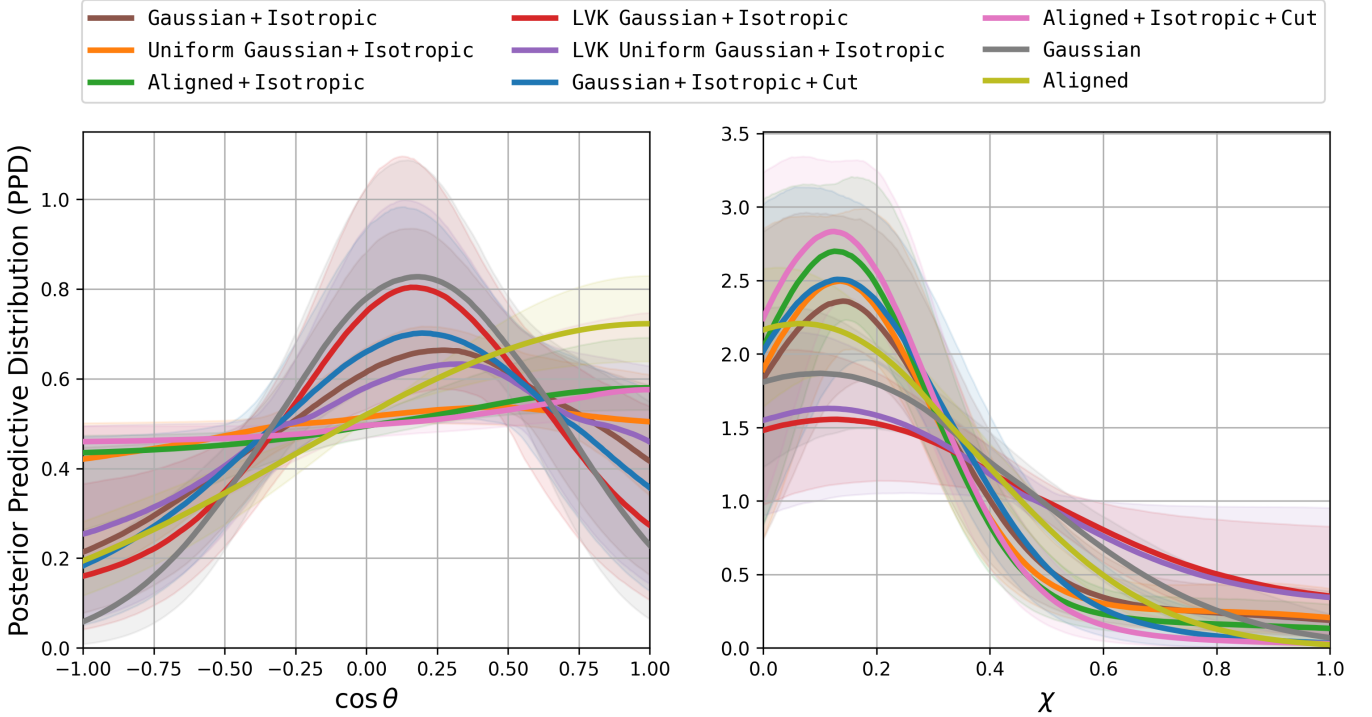


Figure 10. PPDs of the spin-orbit tilt angles (left panel) and spin magnitudes (right panel) across different models. In all models we show the Gaussian + Isotropic mixture (except for the single-component models **Gaussian** and **Aligned**).

- Kass, R. E., & Raftery, A. E. 1995, *Journal of the American Statistical Association*, 90, 773.
<http://www.jstor.org/stable/2291091>
- Klencki, J., Podsiadlowski, P., Langer, N., et al. 2025, arXiv e-prints, arXiv:2505.08860, doi: 10.48550/arXiv.2505.08860
- Kozai, Y. 1962, *Astron. J.*, 67, 591, doi: 10.1086/108790
- Li, Y.-J., Wang, Y.-Z., Tang, S.-P., & Fan, Y.-Z. 2024, *PhRvL*, 133, 051401, doi: 10.1103/PhysRevLett.133.051401
- Lidov, M. L. 1962, *Planet. Space Sci.*, 9, 719, doi: 10.1016/0032-0633(62)90129-0
- Liu, B., & Lai, D. 2018, *Astrophys. J.*, 863, 68, doi: 10.3847/1538-4357/aad09f
- Liu, B., Lai, D., & Wang, Y.-H. 2019, *Astrophys. J.*, 881, 41, doi: 10.3847/1538-4357/ab2dfb
- Mandel, I., & Broekgaarden, F. S. 2022, *Living Rev. Relativ.*, 25, 1, doi: 10.1007/s41114-021-00034-3
- Mandel, I., Farr, W. M., & Gair, J. R. 2019, *MNRAS*, 486, 1086, doi: 10.1093/mnras/stz896
- Mandel, I., & Igoshev, A. P. 2023, *ApJ*, 944, 153, doi: 10.3847/1538-4357/acb3c3
- Mangipudi, A., Grishin, E., Trani, A. A., & Mandel, I. 2022, *ApJ*, 934, 44, doi: 10.3847/1538-4357/ac7958
- McMillin, P., Wagner, K. J., Ficarra, G., Lousto, C. O., & O’Shaughnessy, R. 2025, arXiv e-prints, arXiv:2507.22862, doi: 10.48550/arXiv.2507.22862
- Miller, S., Callister, T. A., & Farr, W. M. 2020, *ApJ*, 895, 128, doi: 10.3847/1538-4357/ab80c0
- Miller, S. J., Ko, Z., Callister, T., & Chatziioannou, K. 2024, *PhRvD*, 109, 104036, doi: 10.1103/PhysRevD.109.104036
- Moe, M., & Di Stefano, R. 2017, *Astrophys. J. Supp. S.*, 230, 15, doi: 10.3847/1538-4365/aa6fb6
- Morras, G., Pratten, G., & Schmidt, P. 2025, *Orbital eccentricity in a neutron star - black hole binary*, <https://arxiv.org/abs/2503.15393>
- Nagarajan, P., El-Badry, K., Chawla, C., et al. 2025, *PASP*, 137, 044202, doi: 10.1088/1538-3873/adc839
- Naoz, S. 2016, *Annu. Rev. Astron. Astrophys.*, 54, 441, doi: 10.1146/annurev-astro-081915-023315
- Noutsos, A., Kramer, M., Carr, P., & Johnston, S. 2012, *MNRAS*, 423, 2736, doi: 10.1111/j.1365-2966.2012.21083.x
- Noutsos, A., Schnitzeler, D. H. F. M., Keane, E. F., Kramer, M., & Johnston, S. 2013, *MNRAS*, 430, 2281, doi: 10.1093/mnras/stt047
- Offner, S. S. R., Moe, M., Kratter, K. M., et al. 2023, in *Astronomical Society of the Pacific Conference Series*, Vol. 534, *Protostars and Planets VII*, ed. S. Inutsuka, Y. Aikawa, T. Muto, K. Tomida, & M. Tamura, 275. <https://arxiv.org/abs/2203.10066>
- Olejak, A., & Belczynski, K. 2021, *ApJL*, 921, L2, doi: 10.3847/2041-8213/ac2f48
- Olejak, A., Belczynski, K., & Ivanova, N. 2021, *Astron. Astrophys.*, 651, A100, doi: 10.1051/0004-6361/202140520
- Olejak, A., Klencki, J., Vigna-Gomez, A., et al. 2025, arXiv e-prints, arXiv:2511.10728, doi: 10.48550/arXiv.2511.10728
- Olejak, A., Klencki, J., Xu, X.-T., et al. 2024, *A&A*, 689, A305, doi: 10.1051/0004-6361/202450480
- Phukon, K. S., Schmidt, P., Morras, G., & Pratten, G. 2025, arXiv e-prints, arXiv:2512.10803, doi: 10.48550/arXiv.2512.10803
- Plunkett, C., Callister, T., Zevin, M., & Vitale, S. 2026, arXiv e-prints, arXiv:2601.07908, doi: 10.48550/arXiv.2601.07908
- Pratten, G., Schmidt, P., Busicchio, R., & Thomas, L. M. 2020, *Physical Review Research*, 2, 043096, doi: 10.1103/PhysRevResearch.2.043096
- Pratten, G., García-Quirós, C., Colleoni, M., et al. 2021, *PhRvD*, 103, 104056, doi: 10.1103/PhysRevD.103.104056
- Rodriguez, C. L., & Antonini, F. 2018, *Astrophys. J.*, 863, 7, doi: 10.3847/1538-4357/aacea4
- Rodriguez, C. L., Zevin, M., Amaro-Seoane, P., et al. 2019, *Phys. Rev. D*, 100, 043027, doi: 10.1103/PhysRevD.100.043027
- Rodriguez, C. L., Zevin, M., Pankow, C., Kalogera, V., & Rasio, F. A. 2016, *ApJL*, 832, L2, doi: 10.3847/2041-8205/832/1/L2
- Romero-Shaw, I., Lasky, P. D., & Thrane, E. 2022, *Astrophys. J.*, 940, 171, doi: 10.3847/1538-4357/ac9798
- Romero-Shaw, I., Lasky, P. D., Thrane, E., & Calderón Bustillo, J. 2020, *ApJL*, 903, L5, doi: 10.3847/2041-8213/abbe26
- Romero-Shaw, I., Stegmann, J., Morras, G., Dorozsmai, A., & Zevin, M. 2025a, doi: 10.48550/arXiv.2512.16289
- Romero-Shaw, I., Stegmann, J., Tagawa, H., et al. 2025b, *PhRvD*, 112, 063052, doi: 10.1103/jj7m-x66y
- Roulet, J., Chia, H. S., Olsen, S., et al. 2021, *PhRvD*, 104, 083010, doi: 10.1103/PhysRevD.104.083010
- Silber, K., & Tremaine, S. 2017, *Astrophys. J.*, 836, 39, doi: 10.3847/1538-4357/aa5729
- Somiya, K. 2012, *Classical and Quantum Gravity*, 29, 124007, doi: 10.1088/0264-9381/29/12/124007

- Speagle, J. S. 2020, *MNRAS*, 493, 3132, doi: [10.1093/mnras/staa278](https://doi.org/10.1093/mnras/staa278)
- Stegmann, J., & Antonini, F. 2021, *PhRvD*, 103, 063007, doi: [10.1103/PhysRevD.103.063007](https://doi.org/10.1103/PhysRevD.103.063007)
- Stegmann, J., Antonini, F., & Moe, M. 2022a, *Mon. Not. R. Astron. Soc.*, 516, 1406, doi: [10.1093/mnras/stac2192](https://doi.org/10.1093/mnras/stac2192)
- Stegmann, J., Antonini, F., Schneider, F. R. N., Tiwari, V., & Chattopadhyay, D. 2022b, *Phys. Rev. D*, 106, 023014, doi: [10.1103/PhysRevD.106.023014](https://doi.org/10.1103/PhysRevD.106.023014)
- Stegmann, J., & Klencki, J. 2025, *ApJL*, 991, L54, doi: [10.3847/2041-8213/ae055b](https://doi.org/10.3847/2041-8213/ae055b)
- Stegmann, J., Vigna-Gómez, A., Rantala, A., et al. 2024, *Astrophys. J. Lett.*, 972, L19, doi: [10.3847/2041-8213/ad70bb](https://doi.org/10.3847/2041-8213/ad70bb)
- Stevenson, S., Berry, C. P. L., & Mandel, I. 2017, *MNRAS*, 471, 2801, doi: [10.1093/mnras/stx1764](https://doi.org/10.1093/mnras/stx1764)
- Stone, N. C., Metzger, B. D., & Haiman, Z. 2017, *MNRAS*, 464, 946, doi: [10.1093/mnras/stw2260](https://doi.org/10.1093/mnras/stw2260)
- Su, Y., Lai, D., & Liu, B. 2021, *PhRvD*, 103, 063040, doi: [10.1103/PhysRevD.103.063040](https://doi.org/10.1103/PhysRevD.103.063040)
- Talbot, C. 2021, doi: [10.5281/zenodo.5654673](https://doi.org/10.5281/zenodo.5654673)
- Talbot, C., Farah, A., Galadage, S., Golomb, J., & Tong, H. 2025, *Journal of Open Source Software*, 10, 7753, doi: [10.21105/joss.07753](https://doi.org/10.21105/joss.07753)
- Talbot, C., Smith, R., Thrane, E., & Poole, G. B. 2019, *PhRvD*, 100, 043030, doi: [10.1103/PhysRevD.100.043030](https://doi.org/10.1103/PhysRevD.100.043030)
- Talbot, C., & Thrane, E. 2017, *PhRvD*, 96, 023012, doi: [10.1103/PhysRevD.96.023012](https://doi.org/10.1103/PhysRevD.96.023012)
- Tauris, T. M. 2022, *ApJ*, 938, 66, doi: [10.3847/1538-4357/ac86c8](https://doi.org/10.3847/1538-4357/ac86c8)
- Tauris, T. M., Kramer, M., Freire, P. C. C., et al. 2017, *ApJ*, 846, 170, doi: [10.3847/1538-4357/aa7e89](https://doi.org/10.3847/1538-4357/aa7e89)
- The LIGO and Virgo Collaborations. 2022, GWTC-2.1: Deep Extended Catalog of Compact Binary Coalescences Observed by LIGO and Virgo During the First Half of the Third Observing Run - Parameter Estimation Data Release, v2 Zenodo, doi: [10.5281/zenodo.6513631](https://doi.org/10.5281/zenodo.6513631)
- The LIGO, Virgo, and KAGRA Collaborations. 2023a, GWTC-3: Compact Binary Coalescences Observed by LIGO and Virgo During the Second Part of the Third Observing Run — Parameter estimation data release, Zenodo, doi: [10.5281/zenodo.8177023](https://doi.org/10.5281/zenodo.8177023)
- The LIGO, Virgo, and KAGRA Collaborations. 2023b, *Phys. Rev. X*, 13, 011048, doi: [10.1103/PhysRevX.13.011048](https://doi.org/10.1103/PhysRevX.13.011048)
- The LIGO, Virgo, and KAGRA Collaborations. 2025a, arXiv e-prints, arXiv:2508.18083, doi: [10.48550/arXiv.2508.18083](https://doi.org/10.48550/arXiv.2508.18083)
- The LIGO, Virgo, and KAGRA Collaborations. 2025b, arXiv e-prints, arXiv:2508.18082, doi: [10.48550/arXiv.2508.18082](https://doi.org/10.48550/arXiv.2508.18082)
- The LIGO, Virgo, and KAGRA Collaborations. 2025c, GWTC-4.0: Parameter estimation data release, Zenodo, doi: [10.5281/zenodo.17014085](https://doi.org/10.5281/zenodo.17014085)
- The LIGO, Virgo, and KAGRA Collaborations. 2025d, GWTC-4.0 Cumulative Search Sensitivity Estimates, Zenodo, doi: [10.5281/zenodo.16740128](https://doi.org/10.5281/zenodo.16740128)
- The LIGO, Virgo, and KAGRA Collaborations. 2025e, GWTC-4.0: Population Properties of Merging Compact Binaries, Zenodo, doi: [10.5281/zenodo.16911563](https://doi.org/10.5281/zenodo.16911563)
- Tong, H., Galadage, S., & Thrane, E. 2022, *PhRvD*, 106, 103019, doi: [10.1103/PhysRevD.106.103019](https://doi.org/10.1103/PhysRevD.106.103019)
- Tong, H., Fishbach, M., Thrane, E., et al. 2025, arXiv e-prints, arXiv:2509.04151, doi: [10.48550/arXiv.2509.04151](https://doi.org/10.48550/arXiv.2509.04151)
- Vaccaro, M. P., Mapelli, M., Périgois, C., et al. 2024, *Astron. Astrophys.*, 685, A51, doi: [10.1051/0004-6361/202348509](https://doi.org/10.1051/0004-6361/202348509)
- van Son, L. A. C., de Mink, S. E., Renzo, M., et al. 2022, *Astrophys. J.*, 940, 184, doi: [10.3847/1538-4357/ac9b0a](https://doi.org/10.3847/1538-4357/ac9b0a)
- Varma, V., Field, S. E., Scheel, M. A., et al. 2019, *Physical Review Research*, 1, 033015, doi: [10.1103/PhysRevResearch.1.033015](https://doi.org/10.1103/PhysRevResearch.1.033015)
- Vigna-Gómez, A., Grishin, E., Stegmann, J., et al. 2025, *A&A*, 699, A272, doi: [10.1051/0004-6361/202554680](https://doi.org/10.1051/0004-6361/202554680)
- Vitale, S., Biscoveanu, S., & Talbot, C. 2022, *A&A*, 668, L2, doi: [10.1051/0004-6361/202245084](https://doi.org/10.1051/0004-6361/202245084)
- Vitale, S., Lynch, R., Sturani, R., & Graff, P. 2017, *Classical and Quantum Gravity*, 34, 03LT01, doi: [10.1088/1361-6382/aa552e](https://doi.org/10.1088/1361-6382/aa552e)
- Vitale, S., Lynch, R., Veitch, J., Raymond, V., & Sturani, R. 2014, *PhRvL*, 112, 251101, doi: [10.1103/PhysRevLett.112.251101](https://doi.org/10.1103/PhysRevLett.112.251101)
- Vitale, S., & Mould, M. 2025, *PhRvD*, 112, 083015, doi: [10.1103/drsl-n3wz](https://doi.org/10.1103/drsl-n3wz)
- Wang, Y.-Z., Li, Y.-J., Vink, J. S., et al. 2022, *ApJL*, 941, L39, doi: [10.3847/2041-8213/aca89f](https://doi.org/10.3847/2041-8213/aca89f)
- Yang, Y., Bartos, I., Gayathri, V., et al. 2019, *PhRvL*, 123, 181101, doi: [10.1103/PhysRevLett.123.181101](https://doi.org/10.1103/PhysRevLett.123.181101)
- Zeipel, H. V. 1909, *Astronomische Nachrichten*, 183, 345, doi: <https://doi.org/10.1002/asna.19091832202>